Article

Petrogenesis and Tectonic Implications of the Triassic Granitoids in the Ela Mountain Area of the East Kunlun Orogenic Belt

Zhongcui Pan [1,2], Fengyue Sun [1,*], Zhichao Cong [1], Nan Tian [1], Wei Xin [3], Li Wang [1], Yajing Zhang [1] and Dongqian Wu [1]

1   College of Earth Sciences, Jilin University, Changchun 130061, China; panzhongcui2019@163.com (Z.P.);
    congzhichao0211@163.com (Z.C.); tian2016nan@163.com (N.T.); wang10li17@163.com (L.W.);
    yjzhang1985@jlu.edu.cn (Y.Z.); wudongqianruishi@163.com (D.W.)
2   Jilin Institute of Geological Sciences, Changchun 130021, China
3   College of Earth Science and Engineering, Shandong University of Science and Technology,
    Qingdao 266590, China; xinwei3860@163.com
*   Correspondence: sunfengyue2022@163.com

Abstract: The East Kunlun Orogenic Belt is located in the western part of the Central Orogenic Belt of China, with a large number of Triassic igneous rocks parallel to the Paleo-Tethys ophiolite belt, which provides a large amount of geological information for the tectonic evolution of the Paleo-Tethys Ocean. The granitoids studied in this paper are located in the Ela Mountain area in the eastern part of the East Kunlun Orogenic Belt. Zircon U-Pb dating results show that these different types of granitoids were crystallized in the Triassic. The 247.5 Ma porphyritic granites from Zairiri (ZRR) displayed calc-alkaline I-type granite affinities, with the zircon $\varepsilon_{Hf}(t)$ values being mainly positive (-0.5 to $+3.8$, T_{DM2} of 1309–1031 Ma), indicating that they are derived from the partial melting of the juvenile crust and mixed with ancient crustal components. The 236.8 Ma Henqionggou (HQG) granodiorites and 237.5 Ma Daheba (DHB) granodiorites are high-K calc-alkaline I-type granite, and both have mafic microgranular enclaves (MMEs), showing higher and more varied $Mg^{\#}$ (39.73–62.73), combined with their negative Hf isotopes ($\varepsilon_{Hf}(t) = -2.6$ to -1.6, $T_{DM2} = 1430$–1369 Ma), suggesting that their primary magmas were the products of partial melting of the Mesoproterozoic lower crust that mixed with mantle-derived rocks. The 236.4 Ma DHB porphyritic diorites showed characteristics of high-K calc-alkaline I-type granitoids, with moderate SiO_2 contents, medium $Mg^{\#}$ values (40.41–40.65), with the Hf isotopes ($\varepsilon_{Hf}(t) = -2.9$ to -0.5; $T_{DM2} = 1451$–1298 Ma) indistinguishably relative to contemporaneous host granodiorites and MMEs. The petrographic and geochemical characteristics indicate that the porphyritic diorites are the product of well-mixed magma derived from the Mesoproterozoic lower crust and lithospheric mantle. Based on the results of this paper and previous data, the chronology framework of Late Permian– Triassic magmatic rocks in the eastern part of the East Kunlun Orogenic Belt was constructed, and the magmatic activities in this area were divided into three peak periods, with each peak representing an extensional event in a particular tectonic setting, for example, P1 (slab roll-back in subduction period; 254–246 Ma), P2 (slab break-off in transition period of subduction and collision; 244–232 Ma), P3 (delamination after collision; 230–218 Ma).

Keywords: Ela Mountain area; petrogenesis; tectonic implication; East Kunlun Orogenic Belt

1. Introduction

The East Kunlun Orogenic Belt is a typical multi-cycle complex orogenic belt that retains information related to the evolution of the Proto-Teyhys Ocean and the Paleo-Tethys Ocean, and records the information and dynamic process of the formation and evolution of the northern Qinghai–Tibet Plateau. Among them, with the exposure of

voluminous magmatic rocks related to the northward subduction of the Paleo-Tethys Ocean in the Late Paleozoic–Early Mesozoic as the main feature, many scholars have carried out relevant research on this area [1–6]. However, there has been controversy over the origin, petrogenesis, tectonic background, and deep process of the huge granitic magma in the late Permian–Triassic period in the East Kunlun Orogenic Belt at present. In particular, different scholars have different views on the final closure time of the Paleo-Tethys Ocean. For example, (1) some researchers believe that the Paleo-Tethys Ocean in the East Kunlun Orogenic Belt was closed in the late Permian, and the Triassic granites are the products of the post-collision environment [4,7,8]; (2) some have proposed that the Permian–Early Triassic granites were mostly subduction magmatic rocks, and the collision orogenic movement began in the Middle Triassic [1,9]; (3) others have pointed out that the subduction of the Paleo-Tethys Ocean in the East Kunlun Orogenic Belt lasted until the Late Triassic, and the Early–Middle Triassic granite was the product of continental margin arc magmatism under subduction environment [5,6,10]; and (4) some believe that the oceanic basin was not closed in the Late Triassic, and that the Paleo-Tethys oceanic crust continued to subduct, with the Triassic magmatism related to the subduction of the oceanic crust [11,12].

Based on the above problems, we selected the Triassic intermediate-acid intrusive rocks in the Ela Mountain area of the easternmost section of the East Kunlun Orogenic Belt as the research object in this paper. Through detailed field geological investigation and petrography, LA-ICP-MS zircon U-Pb ages, whole-rock major oxides, trace elements, and zircon in situ Lu-Hf isotopes analysis technology, the genesis and evolution of different types of magma with different ages were studied. Combined with the relevant information published by our predecessors, the rock combination, temporal and spatial distribution, and stratigraphic relationship of the igneous rocks in the same period in the region are summarized to explore the formation and tectonic background, and provide more information for the tectonic evolution history of the Paleo-Tethys Ocean.

2. Geology and Sample Descriptions

The East Kunlun Orogenic Belt is located in the western part of the Central Orogenic Belt of China and the northern part of the Qinghai–Tibet Plateau (Figure 1a). It is located in the southern margin of the Qaidam Block and the northern side of the Bayanhar–Songpan–Ganz tectonic belt. It is bounded by the Altun Fault in the west and separated from the West Kunlun, adjacent to the West Qinling Orogenic Belt in the east (Figure 1b). The Ela Mountain area studied in this paper is located at the easternmost end of the East Kunlun Orogenic Belt (Figure 1c).

The Precambrian strata in the study area are less exposed, namely the Paleoproterozoic–Mesoproterozoic Jinshuikou Group, which is a set with a high degree of metamorphism, mainly including granulite, gneiss, and schist [8,13]. The Mesozoic Triassic strata are the most widely exposed strata in the study area (Figure 2a). In addition, a small amount of Permian strata are sporadically exposed, while quaternary systems are mostly distributed on both sides of the surrounding basins and water systems.

The magmatic activity in the study area is extremely intense, and both volcanic and intrusive rocks are widely distributed (Figure 2a). According to the isotope age and the relationship with the formation, the intrusive rocks in the area are mainly in the Triassic. Geological surveys in the field have found that the lithology is mainly composed of granodiorite, monzogranite, a small amount of diorite, and syenogranite. Among these rocks, granodiorites are the most widely exposed, with most of them containing MMEs. In comparison, the (quartz) diorite, monzogranite, and syenogranite are smaller in size, and are produced in association with granodiorite as stocks and dikes. In addition, a small number of mafic-intermediate dikes can be seen sporadically. Volcanic eruption activities in the area are also mainly concentrated in the Triassic period, mainly andesite, rhyolite, and a large number of volcanic clastic rocks of the same period.
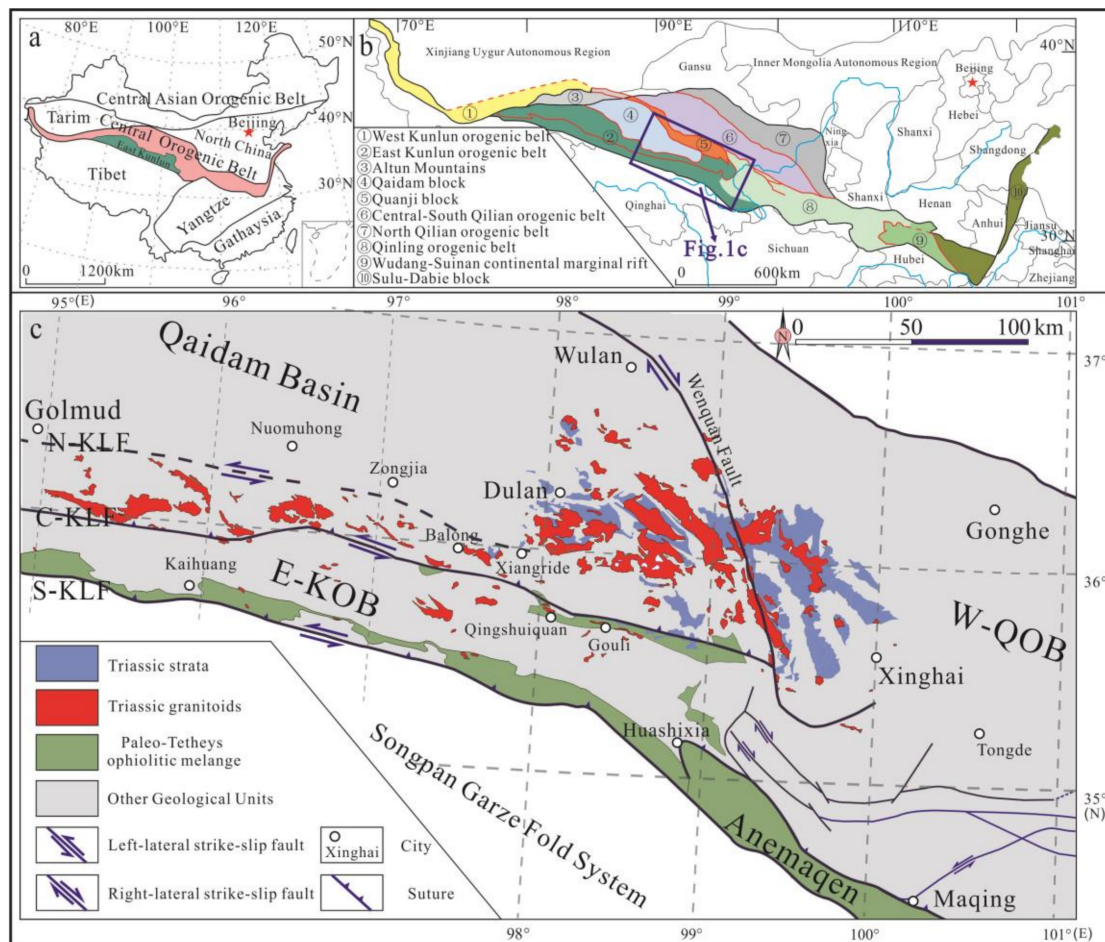
Figure 1. (**a**,**b**) Tectonic map of China revised after [14]. (**c**) Schematic geological map of the Eastern Kunlun Orogenic Belt, N-KLF: North Kunlun Fault; C-KLF: Center Kunlun Fault; S-KLF: South Kunlun Fault; E-KOB: East Kunlun Orogenic Belt; W-QOB: West Qingling Orogenic Belt (simplified and modified after [5,13]).

On the basis of detailed field investigation, we collected porphyritic granites (ZRR-N3), porphyritic diorites (DHB-N5), and granodiorite (DHB-N8 and HQG-N1) samples from three different locations of Zairiri (ZRR), Daheba (DHB), and Henqionggou (HQG) for petrography, LA-ICP-MS zircon U-Pb ages, whole-rock major oxides, trace elements, and zircon in situ Lu–Hf isotopes analysis (Figure 2a,b). The petrographic characteristics of various rocks are described as follows:

Zairiri (ZRR) porphyritic granite: The stock is exposed in the Zairiri region (35°42′08″ N, 99°27′40″ E), which is about 4 km southeast away from Zairigang (Figure 2a). It intruded into the Triassic strata by a small outcrop area (<1 km²) with its south side covered by the Quaternary sediments. The rock is grayish white, porphyritic texture, and massive structure, and the matrix is a microcrystalline structure (Figure 3a). The content of phenocrysts is about 45 vol.%, mainly quartz (25 vol.%), plagioclase (10% vol.%), K-feldspar (5 vol.%), and biotite (5 vol.%). Most of the quartz phenocrysts are melted and eroded in a round shape (Figure 3d). The plagioclase phenocrysts are subeuhedral semiautomorphic in a plate shape, and K-feldspar is irregular granular, biotite in flake, and the particle size of phenocrysts varies from 2 to 12 mm. The matrix accounts for 55 vol.%, mainly composed of feldspar and quartz microcrystals.

Granodiorite plutons: The granodiorites were collected from Daheba (DHB-N8, 35°54′59″ N, 99°36′07″ E) and Henqionggou (HQG-N1, 36°0′09″ N, 99°29′17″ E), respectively, and are part of the Manzhanggang giant granite base (Figure 2a). The macroscopical

characteristics of the rocks are that they both contain mafic microgranular enclaves (MMEs), which are circular and elliptical in shape, with a diameter of 10–200 mm, and the largest of 200–500 mm (Figure 3b). The directional arrangement is not obvious, with a distribution density of 3–5/m^2.

The host granodiorite is grayish white in color, and shows medium grain granite texture and massive structure. The rock is composed of plagioclase (40–50 vol.%), K-feldspar (10–15 vol.%), quartz (20–25 vol.%), hornblende (5–10 vol.%), and biotite (5–10 vol.%), and most mineral particles are between 1–5 mm (Figure 3e). The accessory minerals are magnetite, zircon, sphene, etc. MMEs are fine-grained gabbro-diorite (Figure 3f), which is composed of hornblende (20 vol.%), biotite (15 vol.%), plagioclase (40–45 vol.%), K-feldspar (15–20 vol.%), and a small amount of quartz (5 vol.%). The mineral particles are generally less than 0.5 mm, the accessory minerals are mainly magnets and a small amount of apatite.
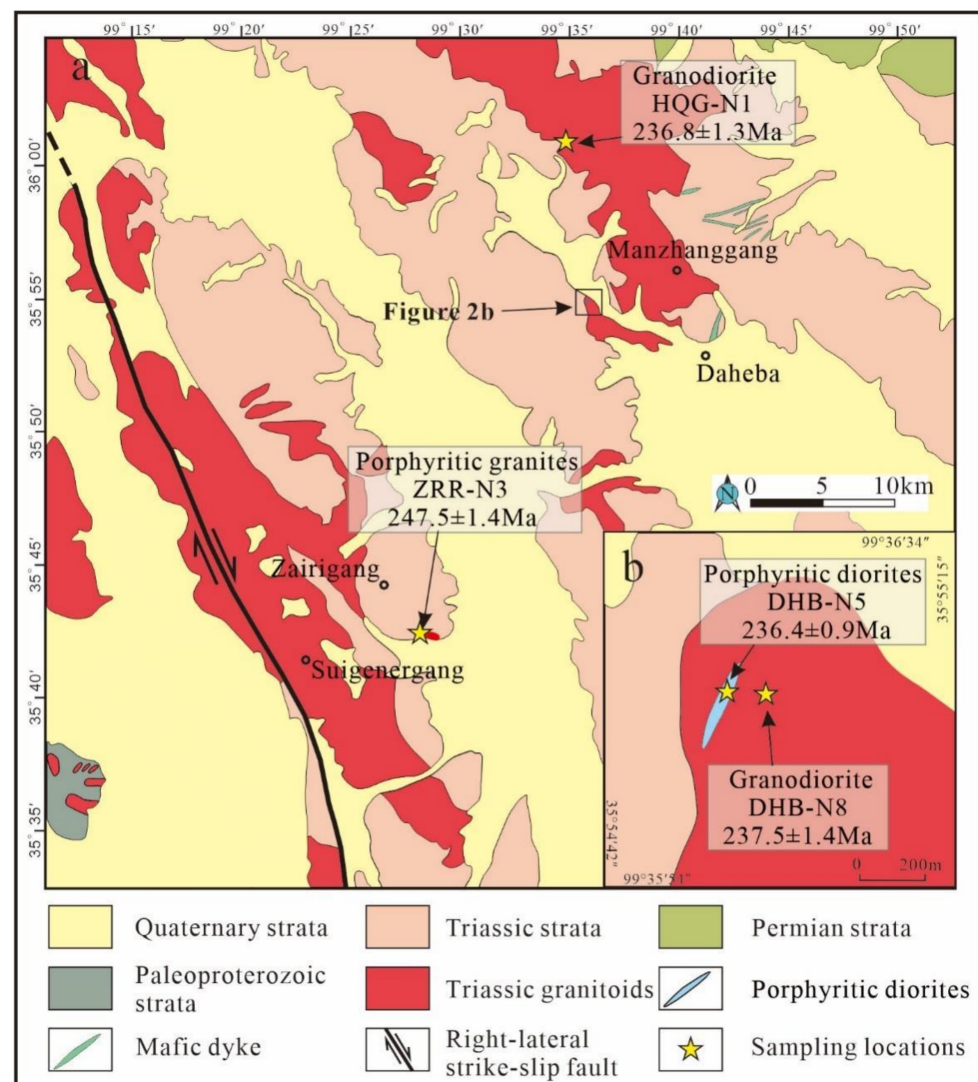

Figure 2. (**a**) Detailed geological map of the Ela Mountain area showing the sampling locations (Modified after 1:250,000 geological maps from the comprehensive geological map of Xinghai and Chaka County, Qinghai Province). (**b**) Detailed geological map of the Daheba area showing the sampling locations (modified after 1:10,000 geological map of Daheba polymetallic mining area in Qinghai Province).
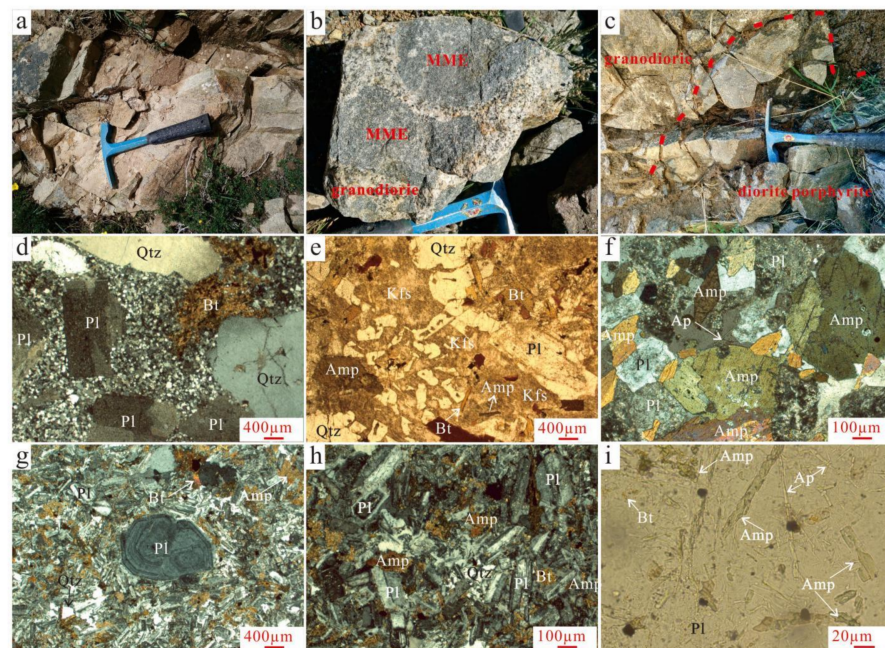
Figure 3. Field photographs and photomicrographs of the intermediate-acid intrusive rocks in the Ela Mountain area. (**a**) Porphyritic granite (field photos). (**b**) Host granodiorite and mafic microgranular enclave (MME) sample (field photos). (**c**) Field contact relationship between granodiorite and porphyritic diorite (field photos). (**d**) Porphyritic granite (cross-polarized light). (**e**) Granodiorite (plane-polarized light). (**f**) MME (cross-polarized light). (**g,h**) Porphyritic diorite (cross-polarized light). (**i**) Porphyritic diorite (plane-polarized light). Mineral abbreviations: Pl, plagioclase; Qtz, quartz; Bt, biotite; Kfs, K-feldspar; Amp, amphibole; Ap, apatite.

Porphyritic diorite: Several diorite dikes can be seen in the study area. The porphyritic diorite (DHB-N5) studied in this paper occurs in the same location as the DHB granodiorite (DHB-N8; 35°54′59″ N, 99°36′07″ E) and intrudes into the granodiorite (Figure 2b). The rock has a porphyritic texture and massive structure (Figure 3g). The content of phenocrysts is less, accounting for about 10 vol.%, mainly plagioclase, and the size of the phenocrysts is between 1 and 2 mm. The matrix content is about 90 vol.%, which is composed of microcrystalline (0.1–0.2mm) feldspar, hornblende, biotite, a small amount of quartz, etc. The accessory minerals are mainly sphene, apatite, magnetite, etc.

3. Analytical Methods

3.1. Zircon U-Pb Dating

The samples used for zircon dating in this paper were all fresh samples collected from natural outcrops. After the samples were broken, washed, and separated, the zircons were manually selected, and zircons with a better crystal form and larger individuals were selected to prepare the sample target. After procedures such as profile cleaning, the zircon samples were tested. Zircon U-Pb isotopic dating and trace element determination using a laser ablation inductively coupled plasma mass spectrometer (LA-ICP-MS), and operated at Yanduzhongshi Geological Analysis Laboratory Ltd., Beijing, China. Helium was used as the carrier gas and argon as the compensation gas to adjust the sensitivity in the process of laser ablation. The analysis data were processed by the software ZSkits (ZSkits 1.1.0, Yanduzhongshi Geological Analysis Laboratory Ltd., Beijing, China). The erosion diameter of this test was 30 μm according to the actual situation of the sample. For the U-Pb isotope dating, the zircon standard 91,500 was used as the external standard for isotope fractionation correction. For each analysis of 5–10 sample points, 91,500 was analyzed twice, and the Plesovice analysis was monitored once. The content of trace elements in zircon was quantitatively calculated using SRM610 as a multi-external standard and Si as

the internal standard [15]. Isoplot/Ex_ver3 [16] was used to draw the U-Pb age concordia diagrams and calculate the average age weight of the zircon samples, and the Andersen (2002) method [17] was used to complete the common lead correction.

3.2. Major and Trace Element Analyses

The major and trace element analysis for the bulk rock samples was carried out at Yanduzhongshi Geological Analysis Laboratories Ltd., Beijing, China. X-ray fluorescence spectrometry techniques were used to analyze the major elements of the whole rock. First, the fresh rocks collected in the field were crushed to centimeters, and then only the rock fragments without alteration and veinless bodies were manually selected from the coarse samples, washed with purified water and dried, and then the samples were crushed to a 200 mesh powder for geochemical testing. The major element test first weighed the powder sample and mixed it with $Li_2B_4O_7$ (1:8) flux, and then heated it to 1150 °C using a melting prototype to melt it into a uniform glass sheet in a platinum crucible, followed by the X-ray fluorescence spectrometry test. The error of the test results was less than 1%.

The trace elements were analyzed using ICP-MS (M90 analytikjena). During the test, a 0.1 g sample was accurately weighed in the polytetrafluoride crucible, 1 mL HF and 3 mL HNO_3 were added, and the crucible was placed on an electric hot plate at 190 °C, heated and steamed to dry, added 20% HNO_3 extract, fixed volume into a 25 mL plastic colorimetric tube, diluted with secondary water, fixed volume to 25 mL, and shaken well. This solution was directly used for the determination of ICP-MS. According to the monitoring standard sample, the GSR-2 displayed an error of the measured data of less than 5%, and the analysis error of some volatile elements and very low content elements was less than 10%. The major and trace element compositions are listed in Table S2.

3.3. Zircon in Situ Lu-Hf Isotopic Analyses

Zircon in situ Lu-Hf isotope dating was completed by an American thermoelectric Nepture-plus MC-ICP-MS and a NewWaveUP213 laser ablation injection system in Yanduzhongshi Geological Analysis Laboratories Ltd., Beijing, China. The test procedure and calibration methods were similar to Wu et al. (2006) [18]. The zircon denudation frequency was 8 Hz, and the energy was 16 J/cm^2 laser denudation 31 s, and the denudation pit was about 43 μm. The diastope interference of ^{176}Lu on ^{176}Hf was negligible. The average ^{173}Yb/^{172}Yb of each test point was used to meter. As the ^{176}Lu/^{177}Hf ratio in zircon is very low (generally less than 0.002), the isotope interference of ^{176}Lu on ^{176}Hf was negligible. The average ^{173}Yb/^{172}Yb of each test point was used to calculate the fractionation coefficient of Yb, and then deducted the isomeric interference of ^{176}Yb on ^{176}Hf. The isotope ratio of ^{173}Yb/^{172}Yb is 1.35274.

4. Results

4.1. Zircon U-Pb Dating

In this study, we collected four samples from different intrusions in the Ela Mountain area for U-Pb dating by LA-ICP-MS. The representative cathodoluminescence (CL) images of the zircons and U-Pb concordia diagrams are shown in Figures 4 and 5, respectively. The U-Pb data are listed in Supplementary Materials Table S1.
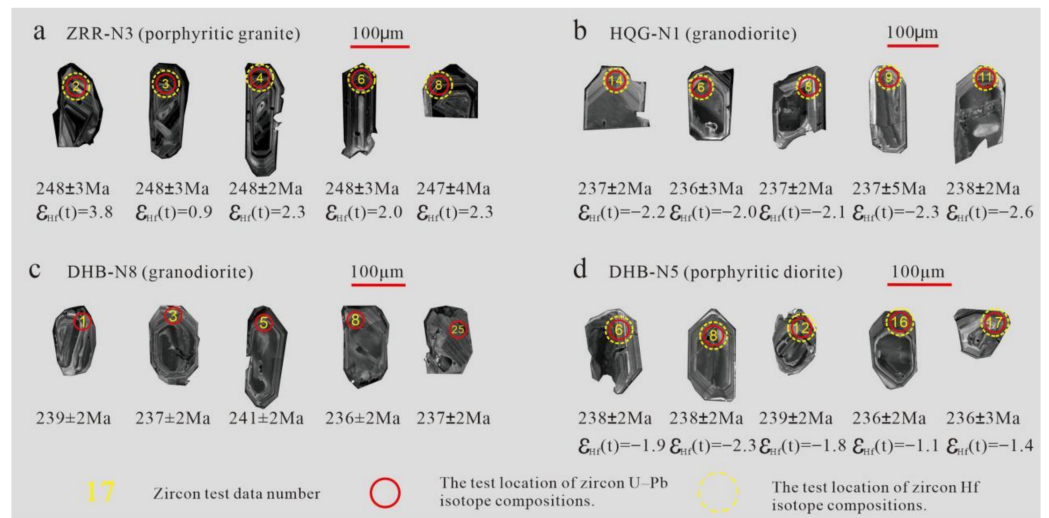
Figure 4. The representative cathodoluminescence (CL) images of zircons from the intermediate-acid intrusive rocks in the Ela Mountain area. Red and yellow circles indicate the locations of the LA-ICP-MS U-Pb analyses and Lu-Hf isotope analyses, respectively. (**a**) The representative CL images of zircons from ZRR-N3 (porphyritic granite). (**b**) The representative CL images of zircons from HQG-N1 (granodiorite). (**c**) The representative CL images of zircons from DHB-N8 (granodiorte). (**d**) The representative CL images of zircons from DHB-N5 (porphyritic dirorite).
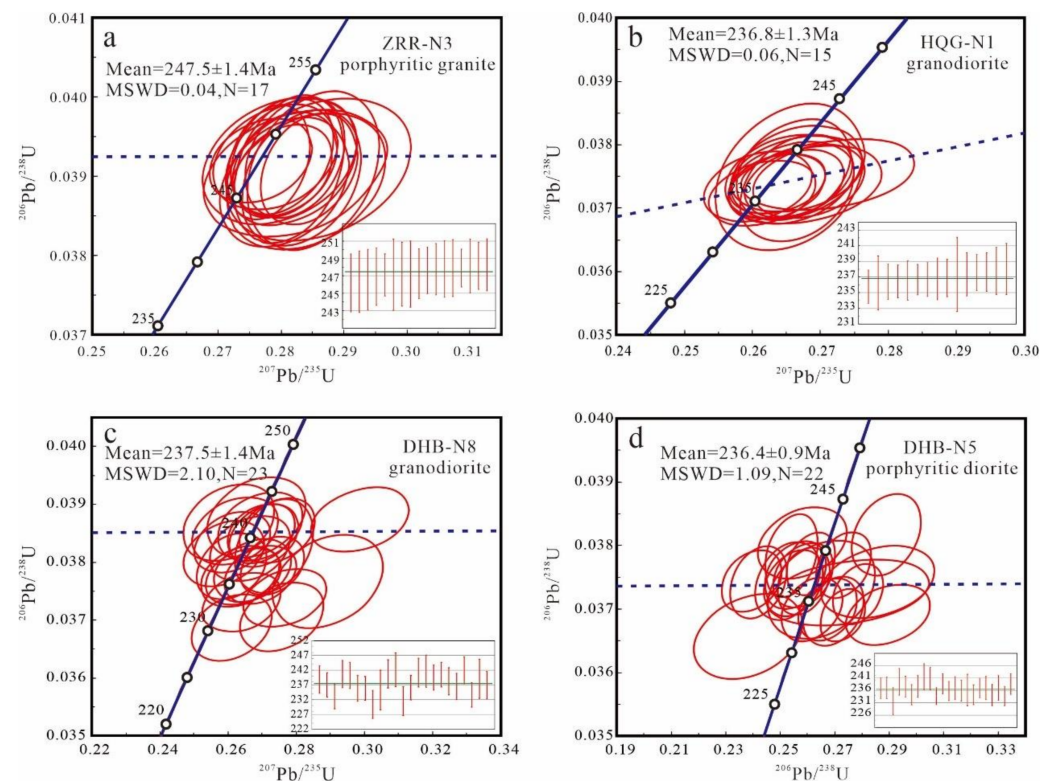

Figure 5. The zircon LA-ICP-MS U-Pb concordia diagrams for the intermediate-acid intrusive rocks in the Ela Mountain area. Weighted-mean ages are shown in each panel. (**a**) The zircon LA-ICP-MS U-Pb concordia diagrams and weighted-mean ages for ZRR-N3 (porphyritic granite). (**b**) The zircon LA-ICP-MS U-Pb concordia diagrams and weighted-mean ages for HQG-N1 (granodiorite). (**c**) The zircon LA-ICP-MS U-Pb concordia diagrams and weighted-mean ages for DHB-N8 (granodiorte). (**d**) The zircon LA-ICP-MS U-Pb concordia diagrams and weighted-mean ages for DHB-N5 (porphyritic dirorite).

Zircons from porphyritic granite (ZRR-N3), porphyritic diorite (DHB-N5), and granodiorite (DHB-N8 and HQG-N1) are colorless transparent to light gray transparent, euhedral-subhedral, mostly columnar in shape, with a size range of 80–300 um, and a length/width ratio of 1:1–3:1. All of the samples showed clear oscillatory growth zoning on the CL images (Figure 4), and had high Th/U ratios of 0.28 to 1.12, indicating magmatic origin [19–21], which can represent their crystallization ages.

A total of twenty spots were analyzed on zircon grains from the sample ZRR porphyritic granite (ZRR-N3). Two spots displayed an older age that would be the earlier zircons trapped in the magma rising process, and one spot displayed obvious Pb loss. The remaining seventeen concordant data points yielded a weighted mean $^{206}Pb/^{238}U$ age of 247.5 ± 1.4 Ma with MSWD = 0.04, which represents the crystallization age of the porphyritic granite (Figure 5a).

Twenty spots were analyzed on zircon grains from HQG granodiorite (HQG-N1). Four spots deviate from the concordia curve, and one older age that would be the earlier zircons trapped in the magma rising process. The remaining fifteen concordant data points yielded a weighted mean $^{206}Pb/^{238}U$ age of 236.8 ± 1.3 Ma with MSWD = 0.06, which represents the crystallization age of the Henqionggou granodiorite (Figure 5b).

Twenty-five spots were analyzed on zircon grains from DHB granodiorite (DHB-N8). One spot deviated from the concordia curve, and one spot displayed obvious Pb loss. The remaining twenty-three concordant data points yielded a weighted mean $^{206}Pb/^{238}U$ age of 237.5 ± 1.4 Ma with MSWD = 2.10, which represents the crystallization age of Daheba granodiorite (Figure 5c).

Twenty-four spots were analyzed on zircon grains from the sample DHB porphyritic diorite (DHB-N5). One spot displayed an older age that would be the earlier zircons trapped in the magma rising process, and one spot deviated from the concordia curve. The remaining twenty-two concordant data points yielded a weighted mean $^{206}Pb/^{238}U$ age of 236.4 ± 0.9 Ma with MSWD = 1.09, which represents the crystallization age of the porphyritic diorite (Figure 5d).

4.2. Whole-Rock Geochemistry

Samples from the ZRR porphyritic granite had a high content of SiO_2 (72.09–73.95 wt.%), Na_2O (3.23–4.12), and K_2O (3.05–3.17 wt.%), low $Fe_2O_3^T$ of 2.19–2.75 wt.%, CaO of 1.19–1.53 wt.%, P_2O_5 of 0.068–0.072 wt.%, TiO_2 of 0.27–0.28 wt.%, and MgO of 0.64–0.75 wt.%, with $Mg^{\#}$ of 33.70–37.25. All of the samples were categorized into calc-alkaline series (Figure 6a,b,d), with Na_2O/K_2O of 1.02–1.35 and $(Na_2O + K_2O)/Al_2O_3$ of 0.48–0.52. The rocks have Al_2O_3 of 13.35–13.83 wt.%, and belong to peraluminous (Figure 6c) with A/NK ratios ranging from 1.37 to 1.52 and A/CNK ratios between 1.13 and 1.16. In the chondrite-normalized REE diagram, the porphyritic granites were enriched in LREEs and depleted in HREEs (Figure 7a) with $(La/Yb)_N$ ratios of 14.72–17.16. All of the samples displayed medium negative Eu anomalies (Eu/Eu* = 0.61–0.63). In the primitive mantle-normalized trace element diagram (Figure 7b), the samples were relatively enriched in some LILEs (e.g., Rb, Th, U, K, and Pb), and depleted in some HFSEs (e.g., Nb, Ta, P, and Ti).

The granodiorites (DHB and HQG) had a SiO_2 content of 65.68–67.95 wt.%, with $Na_2O + K_2O$ of 6.38–7.09 wt.%, ranging from the calc-alkaline to high-k calc-alkaline series (Figure 6a,b,d). The content of MgO was 1.37–1.85 wt.%, and the value of $Mg^{\#}$ varied widely, ranging from 39.58 to 62.73. The rocks belong to the metaluminous to slightly peraluminous (Figure 6c) and had an Al_2O_3 of 14.61–16.19 wt.%. The granodiorites showed the characteristic of being enriched in LREEs and depleted in HREEs (Figure 7c) with $(La/Yb)_N$ ratios of 4.42–20.30. The samples displayed medium to weak negative Eu anomalies (Eu/Eu* = 0.58–0.98). In the primitive mantle-normalized trace element diagram (Figure 7d), the samples were relatively enriched in some LILEs (e.g., Rb, Th, U, K, and Pb), and depleted in some HFSEs (e.g., Nb, Ta, P, and Ti).
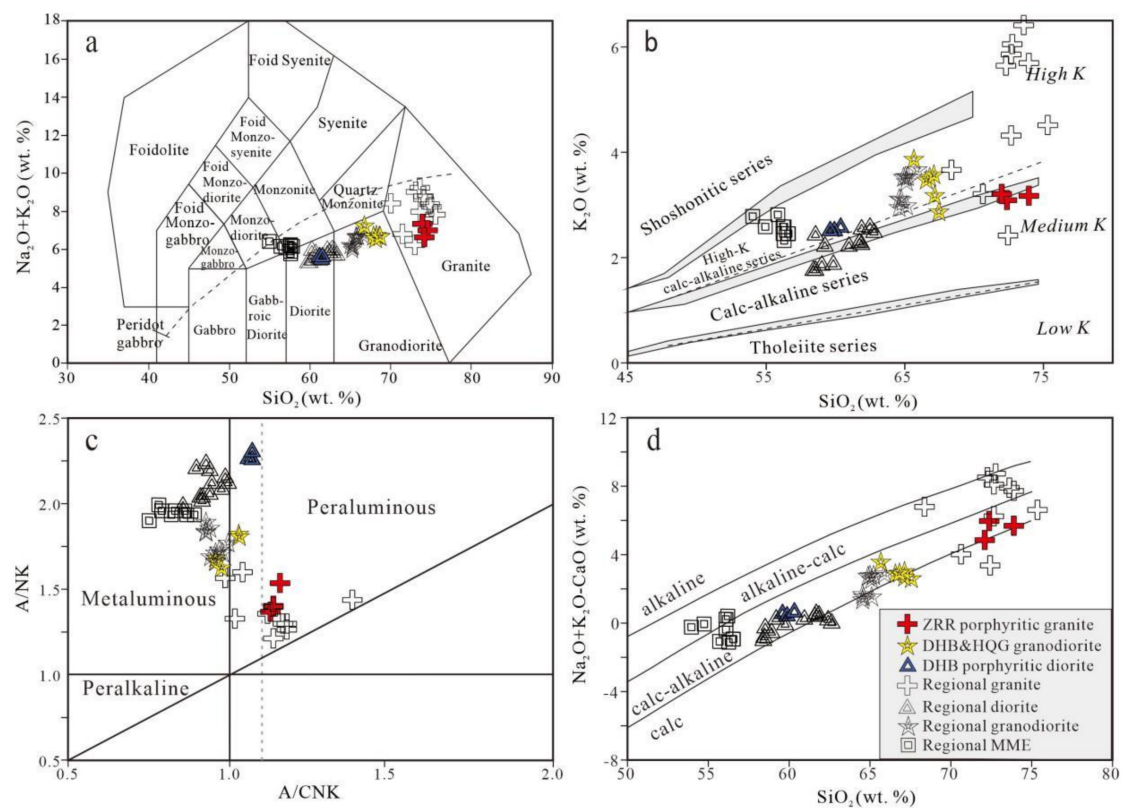
Figure 6. The geochemical classification for the intermediate-acid intrusive rocks in the Ela Mountain area. (**a**) Total alkali versus SiO$_2$ (TAS) diagram [22]; (**b**) SiO$_2$ versus K$_2$O diagram [23] (**c**) A/NK versus A/CNK diagram (A/NK = Al$_2$O$_3$/(Na$_2$O + K$_2$O) molar, A/CNK = Al$_2$O$_3$/(CaO + Na$_2$O + K$_2$O) molar [24]; (**d**) (Na$_2$O + K$_2$O − CaO) versus SiO$_2$ diagram [25]. Data sources: The data for Regional granite were from [1,4], and they indicate previous granites of the same period of the ZRR porphyritic granites (252–247 Ma) in the east section of the East Kunlun Orogenic Belt; the data for Regional granodiorite were from [2,5], and they indicate previous granodiorites of the same period of the DHB and HQG granodiorites (241–235 Ma) in the east section of the East Kunlun Orogenic Belt; the data for regional diorite were from [1–3], and they indicate previous diorites of the same period of the DHB porphyritic diorites (241–235 Ma) in the east section of the East Kunlun Orogenic Belt; the data for MME were from [2,5], and they indicate previous MMEs of the same period of the DHB porphyritic diorite (241–235 Ma) in the east section of the East Kunlun Orogenic Belt.

The DHB porphyritic diorites had a medium SiO$_2$ (59.96–60.41 wt.%), Na$_2$O (2.97–3.06 wt.%), and K$_2$O (2.52–2.59 wt.%), belonging to high-K calc-alkaline series (Figure 6b). They exhibited a moderate MgO of 2.27–2.35 wt%, with a uniform Mg$^{\#}$ value of 40.41–40.65. The rocks were slightly peraluminous with an A/CNK of 1.06–1.07 (Figure 6c). In the chondrite-normalized REE diagram, the porphyritic diorites were enriched in LREEs and depleted in HREEs (Figure 7e) with (La/Yb)$_N$ ratios of 14.72–17.16. All samples displayed medium to weak negative Eu anomalies (Eu/Eu* = 0.78–0.89). In the primitive mantle-normalized trace element diagram (Figure 7f), the samples were relatively enriched in some LILEs (e.g., Rb, Th, U, K, and Pb), and depleted in some HFSEs (e.g., Nb, Ta, P, and Ti).
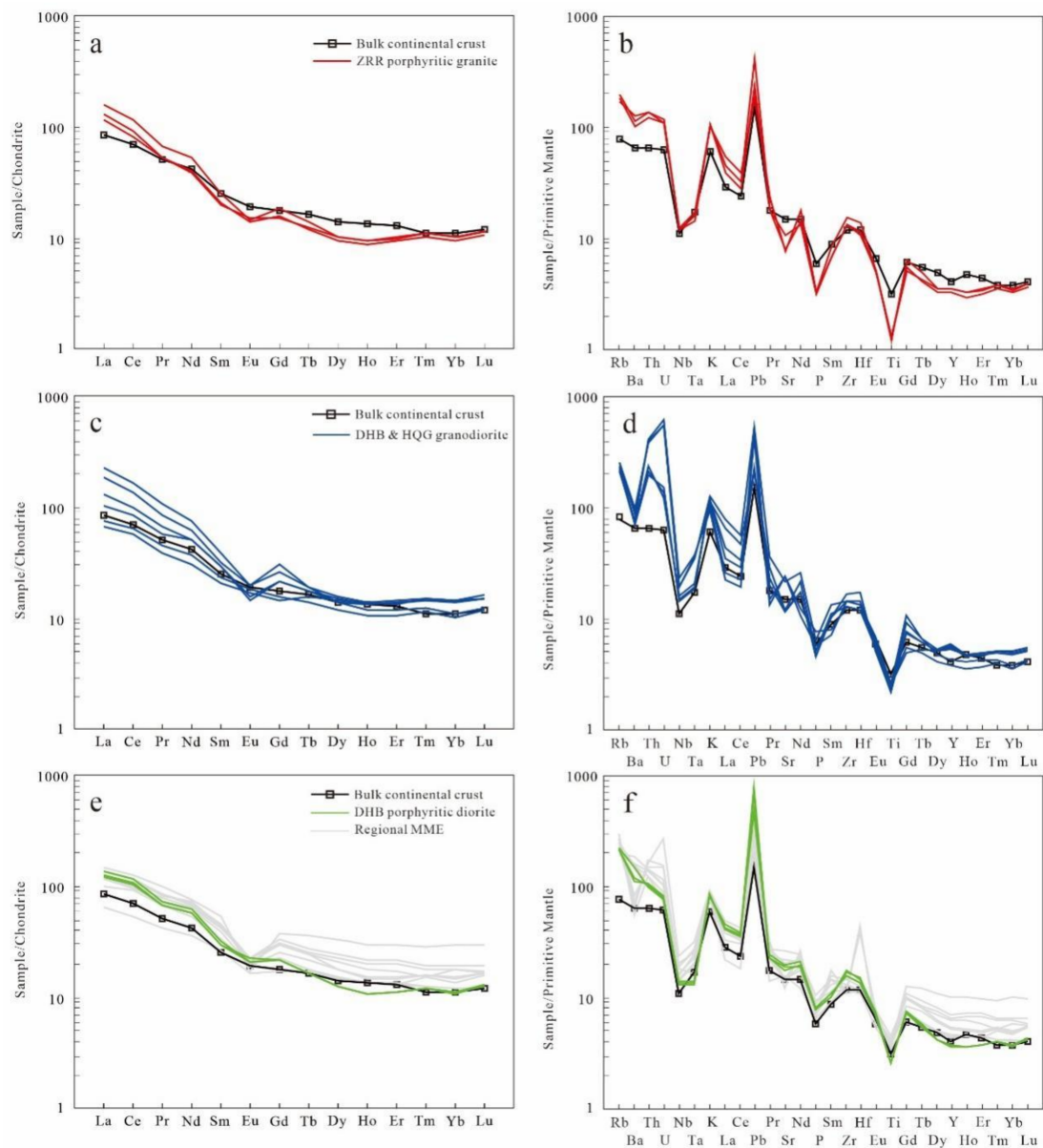
Figure 7. The chondrite-normalized REE patterns and primitive mantle-normalized spider diagrams of trace elements. (**a**,**b**) ZRR porphyritic granites; (**c**,**d**) DHB and HQG granodiorite; (**e**,**f**) DHB porphyritic diorite, the grey line for regional MMEs were from [2,5], and they indicate previous MMEs of the same period of the DHB porphyritic diorites (241–235 Ma) in the east section of the East Kunlun Orogenic Belt. The chondrite values were from [26]. The primitive mantle values were from [27]. The bulk continental crust values were from [28].

4.3. Zircon Hf Isotopic Compositions

The $^{176}Hf/^{177}Hf$ ratio of ZRR porphyritic granites (ZRR-N3, n = 12) in zircon was 0.282609–0.282733, the $\varepsilon_{Hf}(t)$ value was mainly positive (Table S3), which was −0.5 to 3.8, and the two-stage model age (T_{DM2}) was 1309–1031 Ma. The zircons of HQG granodiorites (HQG-N1, n = 10) had $^{176}Hf/^{177}Hf$ ratios of 0.282561–0.282662, $\varepsilon_{Hf}(t)$ values of −2.6 to −1.6 with a T_{DM2} of 1430 to 1369 Ma. The zircon $^{176}Hf/^{177}Hf$ ratio of the DHB porphyritic diorites (DHB-N5, n = 11) was 0.282547–0.282614, and $\varepsilon_{Hf}(t)$ was −2.9 to −0.5 with T_{DM2} of 1451–1298 Ma (Figure 8a,b).
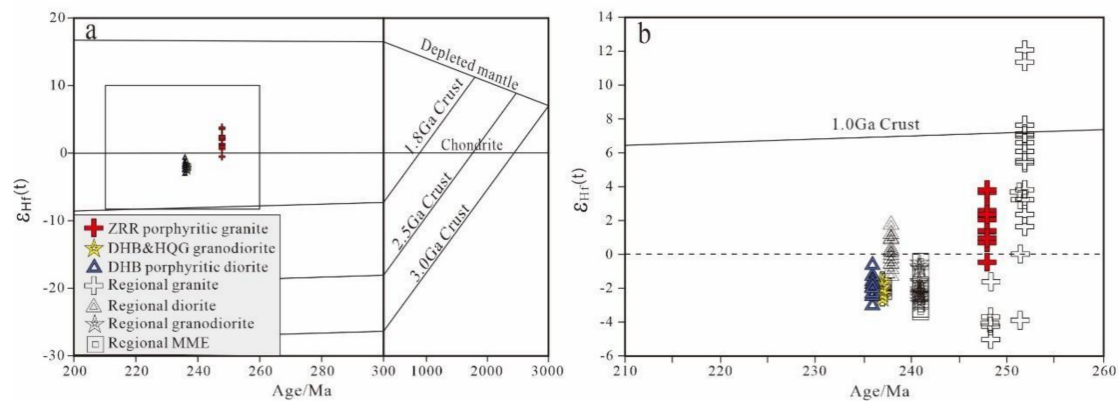
Figure 8. (**a**) Diagram of the zircon $\varepsilon_{Hf}(t)$ versus ages for the granotoids in the Ela Mountain area (this study). (**b**) Plot of the zircon $\varepsilon_{Hf}(t)$ versus ages for the intermediate-acid intrusive rocks in the Ela Mountain area (the sources of the published data are the same as those in Figure 6).

5. Discussion

5.1. Magmatic Process and Petrogenesis

5.1.1. ZRR Porphyritic Granites

Granites are usually divided into I, S, A, and M types according to their mineral composition, chemical composition, source rock characteristics, and tectonic environment [29–37].

M-type granite is mainly related to mantle-derived magma and generally occurs in oceanic crust-type ophiolite suite, mostly plagiogranite, associated with basalt, which is derived directly from the melting of the mantle [33,38,39]. Igneous rocks in the study area are mainly intermediate-acid volcanic rocks and intrusive rocks, and basalts and ophiolites have not been reported. The ZRR porphyritic granite is obviously not the M-type.

Generally, the A-type granite is characterized by alkaline mafic minerals, with high $Na_2O + K_2O$, FeO^T/MgO, $Na_2O + K_2O/CaO$, 10,000 Ga/Al, rare earth content, and high HFSE (e.g., Zr, Nb, Y, Ce, Ga, Zr + Nb + Ce + Y > 350 ppm) in chemical composition [29,30,34,40]. There were no alkaline mafic minerals (e.g., riebeckite, arfvedsonite, sodic pyroxene) in the phenocrysts and matrix of the ZRR porphyritic granites. All samples had a lower FeO^T/MgO (3.00–3.51), $(Na_2O + K_2O)/Al_2O_3$ (0.48–0.52), $(Na_2O + K_2O)/CaO$ (1.70–2.03), 10,000 Ga/Al (2.14–2.16) and relatively low HFSEs content (e.g., Zr (150.17–175.58 ppm); Nb (8.35–8.71 ppm); Y (15.00–16.06 ppm); Ce (50.45–70.38 ppm); Ga (15.14–15.80 ppm); Zr + Nb + Ce + Y (225.71–270.73 ppm), which was obviously different from the A-type granite (Figure 9a–e). The zircon saturation temperature values (T_{Zr}) of the samples were 734–759 °C (Table S2), which were lower than the temperature of the A-type rock (A-type: T_{Zr} > 830 °C) [41,42].

The mafic minerals in the ZRR porphyritic granites were mainly biotite, and there were no characteristic aluminum-rich minerals such as muscovite, garnet, and cordierite of the S-type granite. The Na_2O/K_2O ratio was between 1.02 and 1.35, which shows characteristics of the I-type granite (Figure 9f). The content of P_2O_5 in the samples was 0.060–0.072 wt.%, which was lower than that of S-type granite (>0.1; [43]); the Al_2O_3-SiO_2 and P_2O_5-SiO_2 diagrams (Figure 10g,h) also showed the evolution trend of type I granite [34,44]. Considering that most of the porphyritic granites have the characteristics of calc-alkaline series, we infer that ZRR porphyritic granites are a calc-alkaline I-type granite.
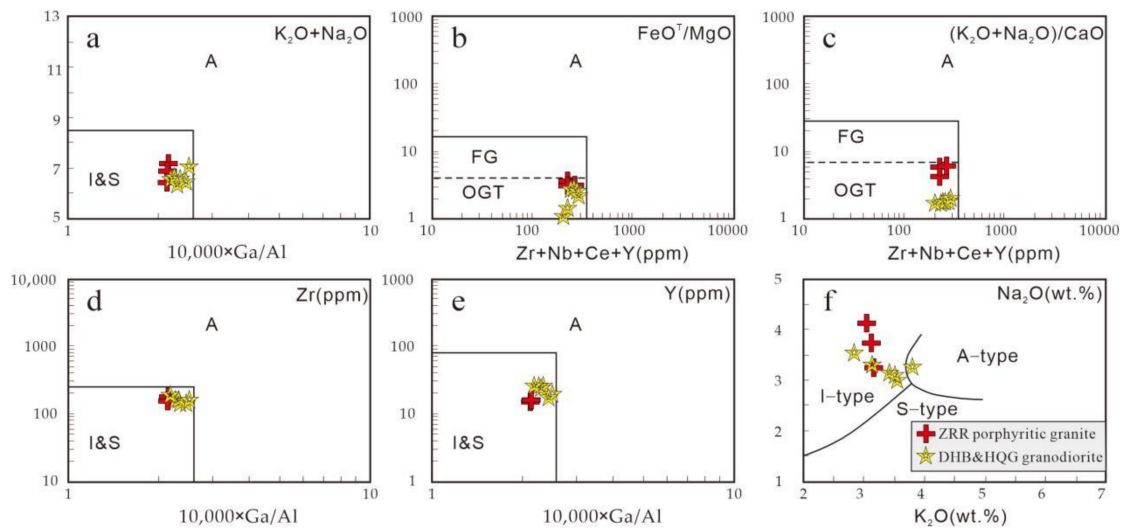
Figure 9. (**a**) (K_2O + Na_2O) versus 10,000 Ga/Al classification diagram; (**b**) FeO^T/MgO versus (Zr + Nb + Ce + Y) classification diagram; (**c**) (K_2O + Na_2O)/CaO versus (Zr + Nb + Ce + Y) classification diagram; (**d**) Zr versus 10,000 Ga/Al classification diagram; (**e**) Y versus 10,000 Ga/Al classification diagram (Figure 9a–e is after [34]); (**f**) Na_2O versus K_2O diagram (after [31]). A: A-type Granites; I&S: I- and S-type Granites; FG: Fractionated Granites; OGT: Unfractionated I and S-type Granites.

In the chondrite-normalized REE diagram and the primitive mantle-normalized trace element diagram, the porphyritic granites showed the characteristics of different extents of Sr, Eu negative anomalies, and strong Nb, Ta, P, Ti negative anomalies (Figure 7a,b), suggesting that there may be mineral separation crystallization during magmatic evolution. They displayed characteristics of the crystallization of feldspar in the Sr–(Rb/Sr) plot (Figure 11a), indicating that there is a separate crystallization of feldspar during magmatic evolution. In the $(La/Yb)_N$-La diagram, there was an obvious evolutionary trend of monazite and allanite (Figure 11b). The depletion of Nb, Ta, and Ti may be related to the separation crystallization of Ti-bearing minerals (Figure 11c). Therefore, in the magmatic evolution process of ZRR porphyritic granites, the separation and crystallization of feldspar and some accessory minerals have an important influence on the change in the element content.

The ZRR porphyritic granites had low MgO (0.64–0.75 wt.%), $Fe_2O_3^T$ (2.19–2.75 wt.%), and MnO (0.64–0.75 wt.%), high SiO_2 (72.09–73.95 wt.%), depleted Nb, Ta, P, Ti, and obvious positive anomalies of Rb, K, Pb, which were similar to the bulk continental crust (BBC) composition (Figure 7b), revealing that their original magma originated from the partial melting of the continental crust [26,46], Nb/Ta between 12.57–14.19, average 13.17, close to the crustal value (13.4; [28]), showing the characteristics of a crustal source [44]. The Hf isotope ratio of zircon usually does not change with partial melting or separation crystallization, so it can be used to trace the magma source properties of granite. The $^{176}Hf/^{177}Hf$ ratio of magmatic zircon in the ZRR porphyritic granites was distributed between 0.282733 and 0.282659, and the $\varepsilon_{Hf}(t)$ value was mainly positive, which was −0.5 to 3.8 (Figure 8). The two-stage model age (T_{DM2}) was 1309–1031 Ma.
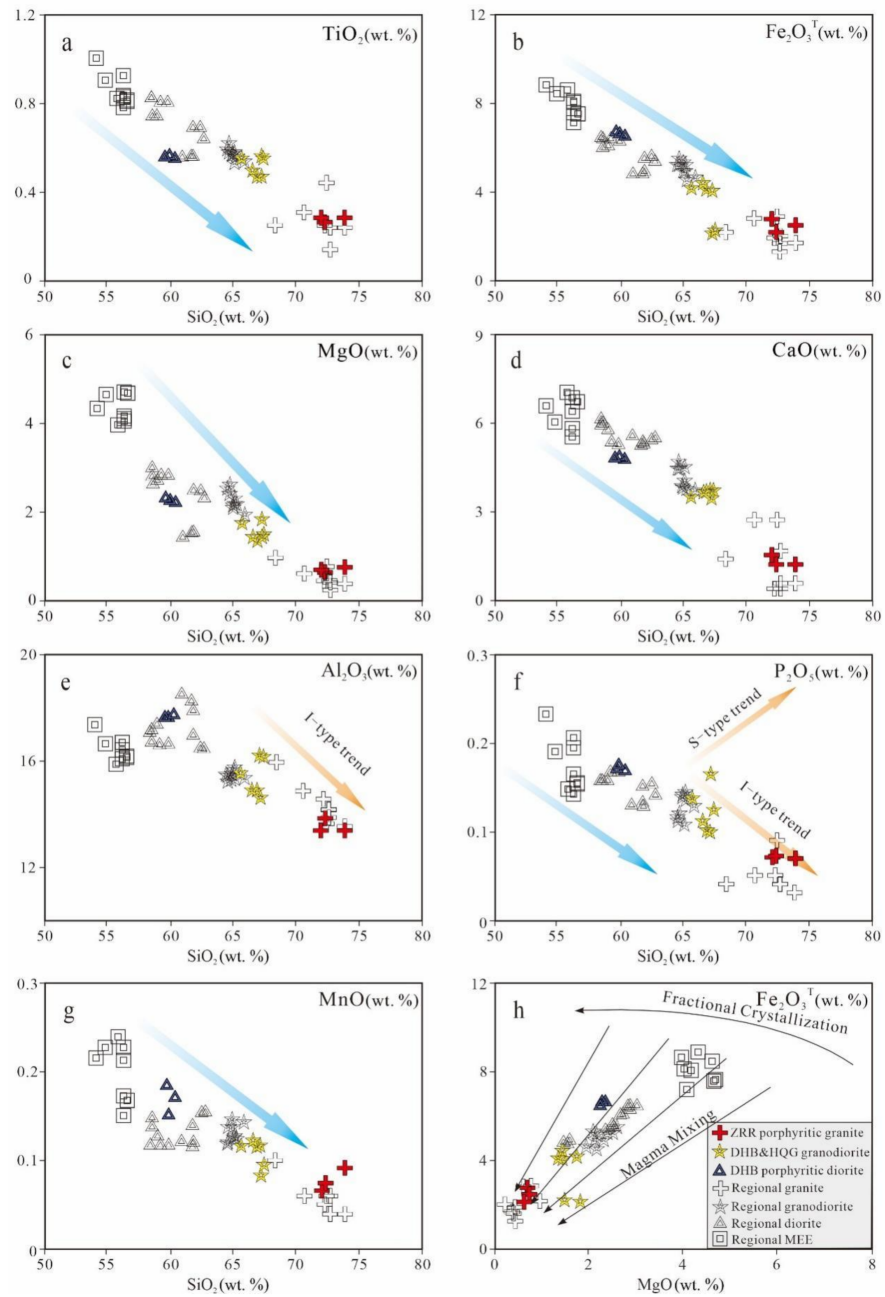
Figure 10. (**a–g**) Harker diagrams for the Triassic igneous rocks in the Ela Mountain area; (**h**) MgO versus Fe₂O₃ᵀ diagram [45]. The sources of published data are the same as those in Figure 6.
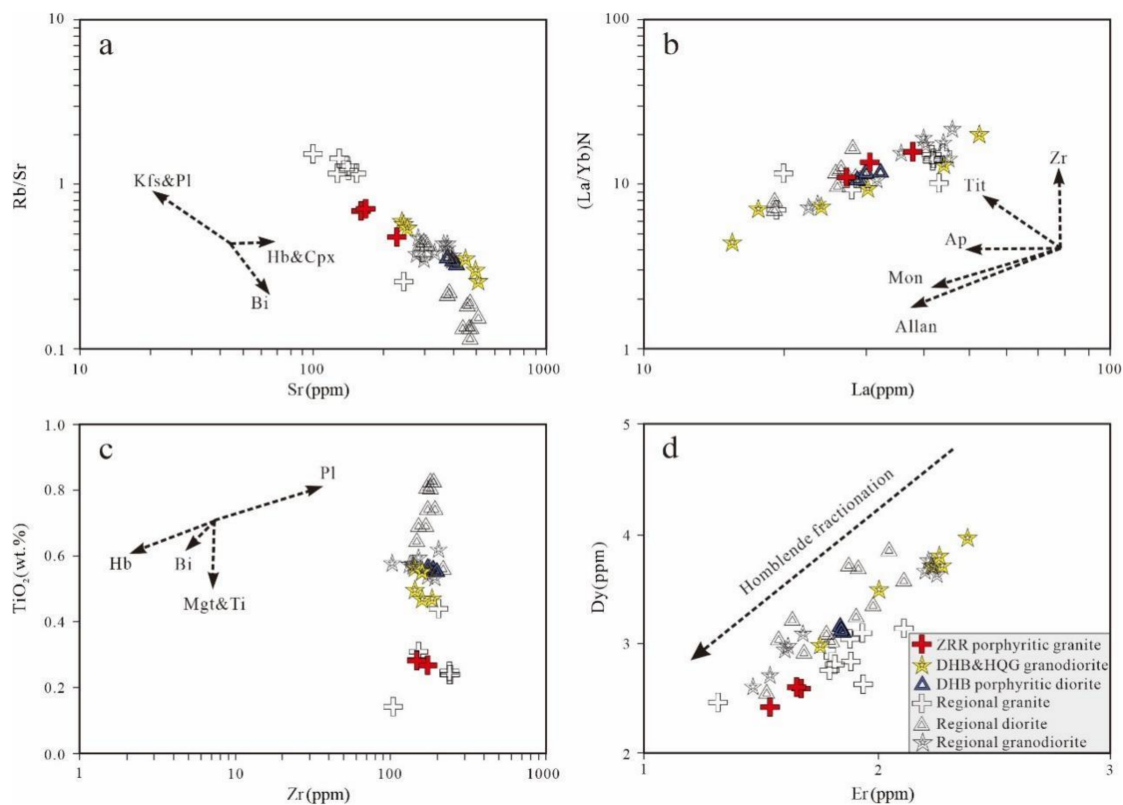
Figure 11. (a) Sr–(Rb/Sr), (b) La–(La/Yb)$_N$, (c) Zr–TiO$_2$, and (d) Er-Dy plots for intermediate-felsic igneous rocks in the Ela Mountain area. Kfs = K-feldspar; Pl = plagioclase; Hb = hornblende; Cpx = clinopyroxene; Bi = biotite; Zr = Zircon; Tit = titanite; Ap = apatite; Mon = monazite; Allan = allanite; Mgt = magnetite. The sources of published data are the same as those in Figure 6.

Another feature of the ZRR porphyritic granites is that it has peraluminous properties. Peraluminous magmatic rocks are generally believed to be formed by extensive deep penetration of surface rocks. However, some peraluminous magmatic rocks can also be formed through the separation and crystallization of hornblende and pyroxene in the closed system by metaluminous magma [47]. Therefore, is the high aluminum saturation index (A/CNK) of the ZRR porphyritic granites a feature of the inherited source area, or is it controlled by the separation and crystallization of hornblende or pyroxene, or caused by the loss of alkali metals caused by late weathering and alteration [48]? The porphyritic granites samples were relatively fresh, the loss on ignition was low (0.54–0.88), and there was no linear relationship between K$_2$O, Na$_2$O, and the loss on ignition (Table S2), indicating that the alteration was not the reason why the rocks had peraluminous characteristics. In addition, all of the samples were sodium-rich, K$_2$O/Na$_2$O < 1, which was obviously different from the typical potassium granite formed by mica dehydration and melting through metamorphic sedimentary rocks (Figure 9i). Hf isotope analysis showed that the porphyritic granites originated from a juvenile crustal source, mixed with a small amount of ancient crustal component (possibly ancient sedimentary metamorphic rocks), and there was a significant positive correlation between Dy and Er (Figure 11d), indicating the existence of separate crystalline phase of amphibole during magmatic evolution [49].

5.1.2. DHB and HQG Granodiorites

The mafic minerals of granodiorites are mainly hornblende, biotite, and magnetite, which are the characteristics of I-type granite [44]. No alkaline mafic minerals or aluminum-rich minerals such as muscovite, garnet and cordierite have been found. The chemical composition of granodiorite is relatively low in SiO$_2$ content (65.68–67.49), FeO^T/MgO (1.06–2.72), (Na$_2$O + K$_2$O)/CaO (1.70–2.03), and the content of HFSEs (Ce, Zr, Nb, Y), is

low, with $Zr + Nb + Ce + Y$ (250.90–296.31), 10,000Ga/Al (2.20–2.46), which is obviously different from that of the A-type granite (Figure 9a–e). In addition, the T_{Zr} values of the samples were 734–759 °C (Table S2), which was lower than the A-type rock (A-type: T_{Zr} > 830 °C; [42]).

The samples of granodiorites had higher contents of Na_2O (3.01–3.54) and CaO (3.50–3.77), Na_2O/K_2O between 0.85 and 1.25, an A/CNK ratio between 0.96 and 1.03 belonging to metaluminous rocks, with a lower Rb/Sr ratio (0.26–0.61), Rb/Ba ratio (0.24–0.30), and higher K/Rb ratio (163.89–209.70), consistent with the I-type granite and different to the S-type granite [34]. The contents of Al_2O_3 and P_2O_5 in the samples were 14.61–16.19 wt.% and 0.10–0.17 wt.%, respectively. The diagram of Al_2O_3-SiO_2 and P_2O_5-SiO_2 (Figure 10e,f) also shows the evolution trend of the I-type granite [34]. Combined with the discussion above and the characteristics of the high-K calc-alkaline of all samples, it is indicated that the granodiorites should belong to the high-K calc-alkaline I-type granite.

There was a negative correlation between the Rb/Sr ratio and Sr of the granodiorite samples (Figure 11a), indicating that there was a separate crystallization of feldspar during magmatic evolution, supported by the negative anomalies of Ba, Sr, and Eu (Figure 7c,d). The trace element diagrams of the granodiorite exhibited significant negative Nb, Ta, P, and Ti anomalies (Figure 7c,d), indicating the fractional crystallization of titanite, allanite, and monazite during magma evolution. In the (La/Yb)$_N$-La diagram (Figure 11b) and the TiO$_2$-Zr diagram (Figure 11c), the evolution trend of the separate crystallization of monazite, allanite, titanite, and magnetite was obvious. The obvious positive correlation between Dy and Er (Figure 11d) indicates that amphibole is the main separated crystalline phase during magmatic evolution. Therefore, the separation and crystallization of feldspar, hornblende, and some accessory minerals occurred in the evolution process of granodiorite magma.

The most prominent feature of DHB and HQG granodiorites is that they both have MMEs. The MMEs are mainly composed of gabbro-diorite, diorite, and monzodiorite. MMEs have different sizes, most of them are several centimeters to dozens of centimeters, and they are oval or muddy in shape (Figure 3b). The boundaries between MMEs and host granodiorites are fuzzy, and they are often in a gradual transition state. Petrography observation showed that the particle size of granodiorite was significantly larger than that of the minerals in MMEs (Figure 3e,f), suggesting that the magma forming of MMEs has the characteristics of rapid cooling. In addition, needle-like structures of minerals such as apatite, hornblende, and biotite are common in MMEs and host granodiorites, which are usually caused by rapid cooling [50,51]. In addition, the large number of needle-like apatites further proved that hot mafic magma was injected into cold siliceous melt [52]. It can be seen that the K-feldspar megacrysts in the host granodiorites contained hornblende, biotite-brown plagioclase, and other sieve structures (Figure 3e). The mafic minerals of hornblende and biotite were clustered and distributed in the cluster structure, and the plagioclase in the host granodiorites and MMEs often had a ring structure with a different composition (Figure 3e,f). These phenomena show the characteristics of magma mixing. The chondrite-normalized REE patterns of granodiorites show that the LREEs were enriched and had a steep right-dipping mode, and the HREEs were depleted but relatively flat on the whole, suggesting that partial melting may occur under the condition of the amphibolite-facies (Figure 7c). The Nb/Ta values of granodiorite samples ranged from 9.26 to 13.38, with an average of 11.68, close to the crustal value (13.4; [28]), showing the characteristics of a crustal source [44]. The Mg$^{\#}$ values from magma of partial melting in the lower crust of basaltic is generally less than 40, and the mixing of mantle-derived melts is generally more than 40 [53]. DHB and HQG granodiorites had high and inhomogeneous MgO (1.37–1.85 wt.%), Mg$^{\#}$ (39.73–62.73 ppm), Cr (14.20–40.85), and Ni (8.49–13.62), which also indicates that the formation of magma may involve the addition of mantle-derived materials. The results of the zircon in situ Hf isotope analysis in granodiorites showed that the $\varepsilon_{Hf}(t)$ value was relatively uniform, and the range of variation was −2.6 to −1.6 (Figure 8). The corresponding two-stage model age (1430–1369 Ma) was nearly consistent with the metamorphic basement age of the lower crust of the eastern part of the East

Kunlun Orogenic Belt (1486–1270 Ma) [54]. Therefore, we can infer that the DHB and HQG granodiorites may be caused by the partial melting of the lower crust, with the mixing of mantle components.

5.1.3. DHB Porphyritic Diorites

Intermediate rock is one of the most important rock types at the edge of the convergent plate, which can provide important information about the crust–mantle interaction and dynamic evolution of the orogenic belt. Therefore, its genesis has always been a hot topic for geologists [2,3,28,55]. At present, a variety of genetic models of intermediate rocks have been proposed including: (1) partial melting of a subduction-modified mantle wedge [56,57]; (2) separating crystallization and crustal contamination of the mantle basaltic magma (assimilation-fractional crystallization process [58,59]); (3) interaction between the subduction slab melt or the thickened lower crust source melt and mantle peridotite [60,61]; (4) partial melting of basaltic rocks in the lower crust [62]; and (5) mixing of basaltic magma and felsic magma [63].

Partial melting of a subduction-modified mantle wedge can form intermediate rocks, but the intermediate magma formed under this mechanism usually has high MgO (>8) and Mg$^\#$ (>65), forming high-Mg intermediate (andesite) magma [56,64]. Compared with the typical high-Mg andesite composition, the DHB porphyritic diorites have lower MgO and Mg$^\#$ (2.27–2.35 and 40.41–40.65, respectively), indicating that the formation of these rocks is not directly formed by the partial melting of subduction-modified mantle wedge. Moreover, the porphyritic diorites have medium SiO$_2$ contents, which are similar to the bulk continental crust, suggesting that the magma source is related to the crust. No crustal xenoliths were found in the porphyritic diorites, and the relatively consistent ε_{Hf}(t) values (−2.9 to −0.5) suggest that the magma is less likely to be contaminated by the crust. Furthermore, significant fractional crystallization would produce significant Eu anomalies because of the removal of plagioclase, which is inconsistent with the DHB porphyritic diorites (Eu/Eu* = 0.78–0.89). Interactions between subduction slab melts or thickened lower crust-derived melts and mantle peridotites tend to form Mg-rich intermediate rocks with adakitic characteristics [60,61]. Compared with typical adakitic intermediate rocks (Figure 12a,b), the DHB porphyritic diorites studied in this paper have relatively low Sr/Y ratios (22.40–24.49) and La/Yb ratios (15.33–17.01). The high K$_2$O/Na$_2$O ratios (0.82–0.85) of the samples are also contradictory to the low K$_2$O/Na$_2$O ratios (<0.5) of adakitic rocks [65]. These characteristics indicate that the DHB porphyritic diorites cannot be a magmatic product of the interaction between subduction slab melt or thickened lower crust source melt and mantle peridotite. Partial melting of basaltic rocks in the lower crust would generate intermediate magma characterized by MgO > 3.0 wt.%, FeO^T > 6.0 wt.%, and TiO$_2$ > 1.0 wt.% [2], which is not quite in accordance with the geochemical characteristics of the DHB porphyritic diorites (MgO of 2.27–2.35 wt.%, FeO^T of 5.93–6.11 wt.%; TiO$_2$ of 0.56–0.57 wt.%). Therefore, we are inclined to think that the porphyritic diorites were formed through magma mixing processes. Here is the following evidence:

First, the DHB porphyritic diorites studied in this paper and the host granodiorites with MMEs occurred in the same place, which is the co-intrusive dyke of granodiorite. The porphyritic diorites are in pulsating intrusive contact with granodiorites. Field observation showed that the contact interface between the porphyritic diorites and granodiorites had a mostly arced or irregular boundary, and the typical necking phenomenon was observed (Figure 3c). The above phenomenon indicates that the host granodiorites is not completely crystallized in the process of dyke emplacement. This was also verified by accurate zircon U-Pb age results. The LA-ICP-MS zircon U-Pb ages of the porphyritic diorites and granodiorites were 236.4 Ma and 236.8 to 237.5 Ma, respectively. These ages are consistent within the error range, showing the same magmatic crystallization products. Second, petrographic observation showed that the mafic minerals such as needle-like hornblende and microcrystal biotite were dispersed in plagioclase large crystals (Figure 3i), which are usually caused by rapid cooling [50,51]; in addition, the large number of needle-

like apatites further proved that hot mafic magma was injected into cold siliceous melt (Figure 3i) [47], suggesting magma mixing. The annular structure and sieve structure of the composition difference of plagioclase in the porphyritic diorites were relatively developed (Figure 3h,i), which indicates that there is a temporary imbalance in the dissolution of Na-rich plagioclase in mafic melt during magma mixing [51], which further indicates magma mixing. Third, in the Harker diagram of the main element, the host granodiorite, MME, and porphyritic diorites showed a good linear variation trend (Figure 10a–g), indicating the characteristics of magma mixing. In the $Fe_2O_3^T$-MgO diagram (Figure 10h), the porphyritic diorites, host granodiorites, and MMEs were along the line of magma mixing. They were also highly consistent in the REE patterns and trace element spider diagrams, indicating that they had strong geochemical affinity and may have had component exchange (Figure 7e,f). In addition, in terms of the trace element ratio, the porphyritic diorites not only showed similar geochemical characteristics to the crust-derived magma, but also had some mantle-derived magma characteristics. The Rb/Sr (0.34–0.37), Ce/Pb (1.17–2.08), and Nb/U (5.64–6.04) were similar to the continental crust (0.35, 4, and 12, respectively) [26], but unconformed with the primitive mantle (0.034, 9 and 30, respectively) [66], indicating that the DHB porphyritic diorites have an affinity with the continental crust. On the other hand, the Nb/Ta value of porphyritic diorites was 17.30–17.64, which is between the continental crust (13.4) [28] and the primitive mantle (17.5) [27], closer to the primitive mantle, and the Zr/Hf value was 39.57–44.55, slightly higher than the primitive mantle value (36.0–37.8) [27] and significantly higher than the continental crust value (33) [67].
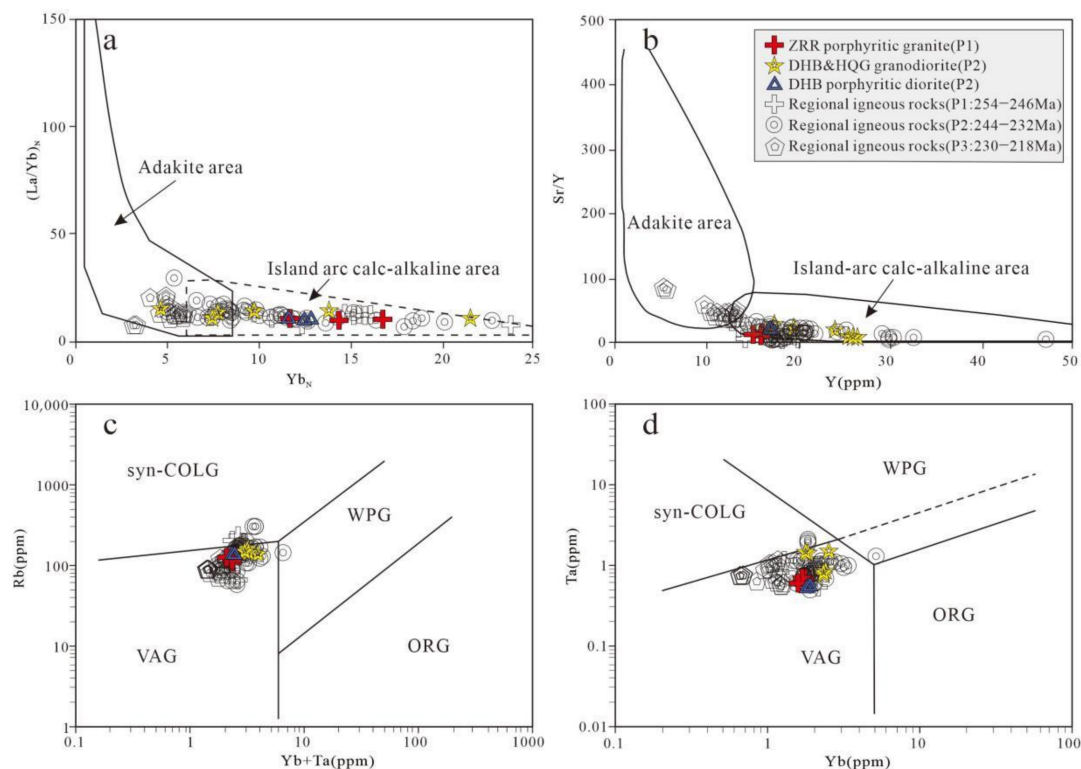

Figure 12. The discrimination diagram of the tectonic environment for early to late Triassic ranitoids in the eastern EKOB. (**a**) $(La/Yb)_N$ versus Yb_N classification diagram [68]; (**b**) Sr/Y versus Y classification diagram [65]; (**c**) Rb versus Yb + Ta diagrams; (**d**) Ta versus Yb diagrams [32]. Abbreviations: syn-COLG = syn-collision granites; VAG = volcanic arc granites; WPG = within plate granites; ORG = ocean ridge granites. Data sources: The data for Regional igneous rocks (P1: 254–246 Ma) were from [1,4]; the data for Regional igneous rocks (P2: 244–232 Ma) were from [1–5,69]; the data for Regional igneous rocks (P3: 230–218Ma) were from [2,9,70].

We infer that the formation of DHB porphyritic diorite and granodiorite experienced different extents of magmatic mixing process. It is an irregular mixing between granodiorites and MMEs, with a small amount of mafic magma injected into granitic magma. Mafic magma generally has a high temperature and low viscosity, and the diffusion coefficient is relatively high, so mafic magma appears commonly as enclaves in the granitic magma [71,72]. The structural characteristics of acicular amphibole, biotite, and apatite crystals that are often formed by accelerating cooling in MMEs and around the contact with host granodiorites indicate the process of high-temperature mafic magma injected into cold and acidic magma. The formation of porphyritic diorites may occur at the contact interface between mafic magma and acidic magma in the magma chamber of deep crust, with relatively complete mixing. The intermediate magma (porphyritic diorites) rapidly rises to the surface in weak structural areas such as fractures generated by the condensation of acidic magma (granodiorite), forming porphyritic diorites.

5.2. Tectonic Implications

We used the zircon U-Pb ages of the four intrusive rocks provided in this paper and the previous research results of magmatic chronology in the eastern part of the East Kunlun Orogenic Belt published in recent years for statistical analysis (Figure 13; Table S4). The age histogram revealed the three peak periods of the Late Permian–Triassic magmatism in the eastern East Kunlun Orogenic Belt, and here we named them as P1 (254–246 Ma), P2 (244–232 Ma), and P3 (230–218 Ma), respectively. According to the age distribution characteristics of these magmatic activities, combined with the rock combination and rock type of each period, we analyzed the magmatic activities distributed in the Late Permian–Triassic in the study area by integrating geological factors such as strata and structures, and found that the emergence of a large number of magmatic rocks in each peak period may correspond to different dynamic mechanisms and backgrounds.
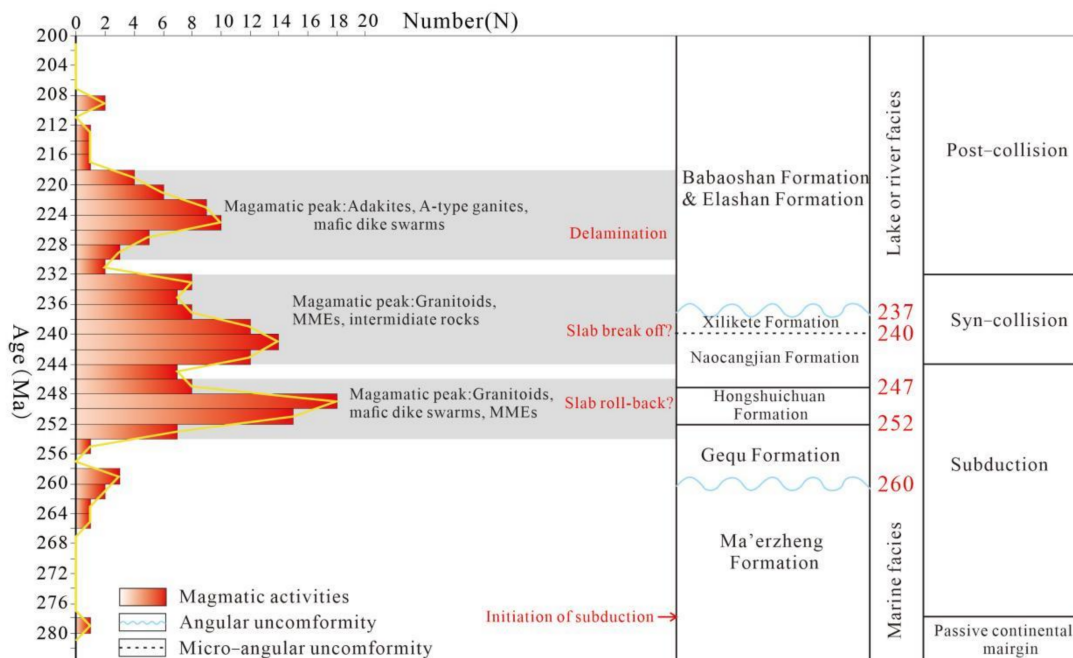

Figure 13. The histograms of ages of the Late Permian-Triassic igneous rocks and strata data in the eastern of the East Kunlun Orogenic Belt. The ages data sources are the same as those in Table S4, and the strata data modified after [69,73].

Studies on ophiolites (308–345 Ma) in the Paleo-Tethys area of the East Kunlun Orogenic Belt suggest that the Paleo-Tethys Ocean basin of East Kunlun began to expand in the Carboniferous [74–76]. The regional angular unconformity of the Upper Permian Gequ

Formation above the Upper Carboniferous Ma'erzheng Formation in the East Kunlun area indicates that regional tectonic disturbance occurred in the Late Permian [73,74]. The Xiaomiao mafic dike swarm at about 278 Ma showed obvious Nb-Ta-Ti depletions with an arc attribute and then the granites with arc characteristics were successively discovered, indicating that the Paleo-Tethys Ocean had begun to subduct in the Late Permian [77,78]. However, during the subsequent 278–254 Ma period, only a small amount of magmatic activity was recorded, which manifested as a stable period of magmatic activity, which may imply a low-angle subduction stage relative to the extrusion environment (Figure 14a; [2]). During the P1 (252–248 Ma) peak period, the first magmatic activity erupted (Figure 13), during which mafic dyke swarms with arc properties [2,79,80] and a large number of calc-alkaline to high-K calc-alkaline intermediate-acid magmatic activities with continental margin arc characteristics were widely developed during this period [1,4,9,81], suggesting extensive crust–mantle interactions in a subduction setting. The mafic dyke swarms of the early Triassic (P1 peak period) are the products of the extensive reworking of the lithospheric mantle, which suggests an asthenospheric upwelling event during this period [2,82]. In the subduction environment, slab roll-back can induce upwelling of the asthenosphere and subsequent massive magmatic activity [2,83]. Therefore, we believe that the magmatic peak of the P1 stage may respond to the roll-back of the subduction slab during the subduction stage (Figure 14b).
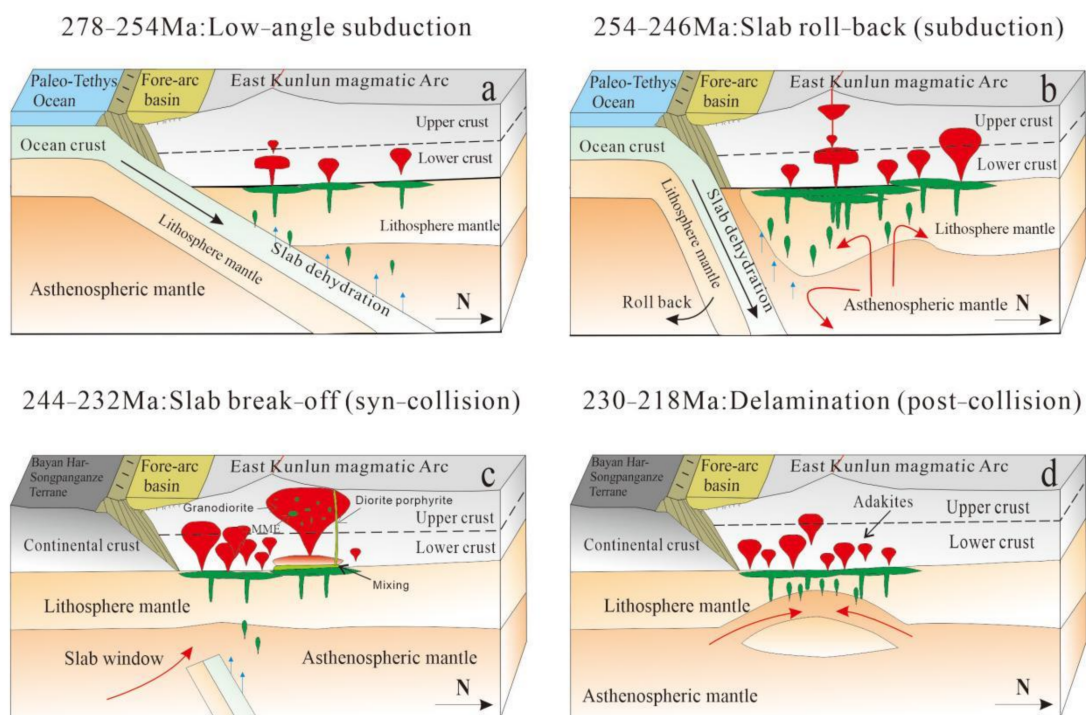

Figure 14. A schematic cartoon illustrating a proposed genetic model for geodynamic evolution in the eastern part of the East Kunlun Orogenic Belt. (**a**) Low-angle subduction; (**b**) slab roll-back; (**c**) slab break-off; (**d**) delamination.

The ZRR porphyritic granites studied in this paper were formed in the early Triassic (P1 peak period), with calc-alkaline characteristics (Figure 6b), enriched LILE and LREE (e.g., Rb, K and Pb), and depleted HREEs and HFSEs (e.g., Nb, Ta Ti and P; Figure 7a,b), similar to the arc-like granite in a subduction environment [84,85]. Additionally, the granitoids in the study area had medium-high Y, Yb values and low $(La/Yb)_N$ and Sr/Y ratios at the P1 peak period, which are similar to the composition of arc-like calc-alkaline rocks (Figure 12a,b), indicating that the granitoids in this period were formed in the active continental margin environment related to the subduction process [84,85]. The average La/Nb ratio of porphyritic granites was 3.73, which is similar to the La/Nb ratio of igneous

rock in the active continental margin area (>2, [86]). In the Ta-Yb and Rb-(Ta + Yb) diagrams, the P1 peak period samples fell into the volcanic arc granite area (Figure 12c,d), which supports that the P1 peak period (254–246 Ma) granitoids belong to the volcanic arc or active continental margin [32].

ZRR porphyritic granites and some other igneous rocks of the P1 peak period (254–246 Ma) in the East Kunlun [1,4] showed a significant mantle contribution (i.e., $\varepsilon_{Hf}(t)$ values are mainly positive (Figure 8)), indicating that the rocks should originate from the depleted mantle source area, but the direct partial melting of the depleted mantle cannot form a high SiO_2 content granitic melt [85]. To produce these intermediate-acid bulk continental crust-like magmas with mantle characteristics, it is necessary to have a basaltic source in addition to some continental materials [4]. This basaltic rock may be derived from the oceanic crust of the depleted mantle or the basalt of the asthenospheric mantle in the source area. In the subduction zone environment, due to the low geothermal gradient, the ordinary subduction oceanic crust cannot be partially melted directly. The partial melting of the mantle wedge enriched by the fluid metasomatism of the subduction oceanic crust will form andesite magma with a relatively low SiO_2 content [85]. If the juvenile subduction oceanic crust (with high low temperature gradient) is directly partially melted, it will form adakite with a high Sr/Y ratio [65]. However, the ZRR porphyritic granites and granites of the same period obviously do not have the geochemical properties of adakite with high Sr and low Y, which cannot be the product of the direct partial melting of the subduction oceanic crust. Therefore, we believe that the possible formation mode of ZRR porphyritic granites is partial melting of the mantle wedge in the early subduction to the bottom of the lower crust, and the upwelling of the asthenosphere in the late subduction stage, resulting in the partial melting of the early juvenile lower crust and a small amount of ancient crustal materials (possibly Al-rich ancient sedimentary rocks). The granitic magma experienced the crystallization differentiation of feldspar and amphibole and finally formed a calc-alkaline I-type granite. In summary, this paper believes that ZRR porphyritic granites are representative of continental arc granite formed in the active continental margin environment during the subduction stage of the Paleo-Tethys Ocean.

P2 (244–232 Ma) is the second period of frequent magmatic activity. The intrusive rocks in this period are mainly granodiorite, monzogranite, syenogranite, and a small amount of diorite and gabbro. Among them, the granodiorite often contains MMEs, and the volcanic rocks are mostly rhyolite, dacite, andesite, and pyroclastic rocks of the same period. The zircon Hf isotope results showed that the magma was mainly derived from the partial melting of the lower crust of the Mesoproterozoic, and some of them mixed with a small amount of mantle material [2,3,5,6]. In terms of sedimentary assemblages, the Middle Triassic Xilikete Formation has the characteristics of marine-continental sedimentary assemblages [73] and an angular unconformity contact with the Late Triassic continental volcanic rocks (Elashan Formation and Babaoshan Formation, Figure 13), indicating that the East Kunlun Orogenic Belt was in a rapid uplift stage during the Middle Triassic, representing the collision between the BayanHar Block and the Eastern Kunlun Block and the disappearance of the Paleo-Tethys Ocean, resulting in local deposition. The intense magmatic activity and crust–mantle magma interaction during this period may have broken-off the subduction slab.

Both the DHB and HQG granodiorites and DHB porphyritic diorites belong to the high-K calc-alkaline series rocks, with similar formation ages and are closely associated in space, and they represent indistinguishable Hf isotopic characteristics (Figure 8), indicating that the magma was mainly formed by partial melting of the lower crust of the Mesoproterozoic. However, field investigation, petrographic study, and the analysis of major and trace elements showed that porphyritic diorites and granodiorites had mixed with the mantle-derived magma to varying degrees. The granodiorite was formed by underplating mantle mafic magma and granitic magma through insufficient mechanical mixing, and MMEs were generally present in the granodiorite. However, porphyritic diorites may be formed in the magma chamber in the deep crust near the contact interface between the mafic

magma and granitic magma after full mixing. These intermediate magma ascended along the fracture space of early unconsolidated granodiorite, experiencing the separation and crystallization of a small amount of plagioclase, biotite, and hornblende minerals before magma emplacement.

In the tectonic discrimination diagrams, a small amount of granite in the same period of P2 (244–232 Ma) fell into the syn-collision environment (Figure 12 c,d). Combined with the stratigraphic and magmatic rock association in the area discussed above, we inferred that at the end of Middle Triassic, the Paleo-Tethys Ocean may have closed in this area. A large number of magmatic activities during this period can be explained by the model of slab break-off (Figure 14c). The break-off of the slab formed a decompressive environment, resulting in the upwelling of the asthenosphere. The mafic magma formed by partial melting of the lithospheric mantle underplated the lower crust, resulting in partial melting of the lower crust and forming granitic magma. A small amount of mafic melt was rapidly injected into granitic magma and mechanically mixed to produce the granodiorites with MMEs. At the contact interface between the mafic magma and granitic magma in the magma chamber of the lower crust, the two magmas were fully mixed to form intermediate magma. The intermediate magma after uniform mixing invades along the unconsolidated granodiorite fracture forming the porphyritic diorite veins (Figure 14c). In this process, mantle magma provides enough heat to enhance crustal deep melting [87]. These diorite and granitic melts move upward, and through the crystallization and differentiation of a small amount of plagioclase, hornblende, and other minerals, the widely distributed granodiorite and a small amount of diorite rock strains and dikes are finally formed.

P3 (230–218 Ma), a large number of mafic dikes [3,88,89] and A-type granites related to extension were formed in the area at this time [90], representing the post-collision extension environment. In addition, lots of adakitic magmatic rocks with high Sr/Y, $(La/Yb)_N$ and low Y, Yb began to appear in the East Kunlun Orogenic Belt (Figure 12a,b) [2,9,70], reflecting that the East Kunlun Orogenic Belt was already in the extensional tectonic background caused by the delamination of the thickened lower crust and lithospheric mantle (Figure 14d). The Sedimentary, Upper Triassic Elashan Formation, and Babaoshan Formation of continental clastic sedimentary combination also confirmed that the East Kunlun Orogenic Belt had fully entered the post-collisional intracontinental environment in the Late Triassic [73,88].

6. Conclusions

The LA-ICP-MS zircon U-Pb geochronology analysis revealed that the crystallization ages of ZRR porphyritic granite, HQG granodiorite, DHB granodiorite, and DHB porphyritic diorites in Ela Mountain area were 247.5 ± 1.4 Ma, 237.5 ± 1.4 Ma, 236.8 ± 1.3 Ma, and 236.4 ± 0.9 Ma, respectively.

The ZRR porphyritic granite belongs to the calc-alkaline I-type granite, which is mainly derived from the partial melting of the juvenile crust and mixed with ancient crustal components. It is the representative of continental arc granite formed in the active continental margin environment during the subduction of the Paleo-Tethys Ocean. The DHB and HQG granodiorites are high-K calc-alkaline I-type granite. The DHB porphyritic diorites had the same crystallization age and similar Hf isotopic composition as the granodiorites in the area. These are mainly formed by partial melting of the lower crust of the Mesoproterozoic, and have undergone different degrees of mixing with mantle-derived magma. They formed in the late Middle Triassic, at the environment of slab-break off in the transition period of subduction and collision.

The three magmatic peaks of P1 (254–246 Ma), P2 (244–232 Ma), and P3 (230–218 Ma) in the East Kunlun Orogenic Belt corresponded to three extensional events, respectively, P1—slab roll-back in subduction period; P2—slab break-off in transition period of subduction and collision; and P3—delamination after collision.

References

1. Ren, H.D.; Wang, T.; Zhang, L.; Wang, X.X.; Huang, H.; Feng, C.Y.; Teschner, C.; Song, P. Ages, Sources and Tectonic Settings of the Triassic Igneous Rocks in the Easternmost Segment of the East Kunlun Orogen, central China. *Acta Geol. Sin.-Engl. Ed.* **2016**, *90*, 641–668.

2. Xin, W.; Sun, F.Y.; Zhang, Y.T.; Fan, X.Z.; Wang, Y.C.; Li, L. Mafic–intermediate igneous rocks in the East Kunlun Orogenic Belt, northwestern China: Petrogenesis and implications for regional geodynamic evolution during the Triassic. *Lithos* **2019**, *346*, 105159. [CrossRef]

3. Wu, D.Q.; Sun, F.Y.; Pan, Z.C.; Tian, N. Geochronology, geochemistry, and Hf isotopic compositions of Triassic igneous rocks in the easternmost segment of the East Kunlun Orogenic Belt, NW China: Implications for magmatism and tectonic evolution. *Int. Geol. Rev.* **2021**, *63*, 1011–1029. [CrossRef]

4. Kong, J.J.; Niu, Y.L.; Hu, Y.; Zhang, Y.; Shao, F.L. Petrogenesis of the Triassic granitoids from the East Kunlun Orogenic Belt, NWChina: Implications for continental crust growth from syn-collisional to post-collisional setting. *Lithos* **2020**, *364*, 105513. [CrossRef]

5. Tian, N.; Sun, F.Y.; Pan, Z.C.; Li, L.; Gu, Y.; Wu, D.Q.; Deng, J.F.; Liu, Z.D.; Wang, L.; Zhang, Y.J. Triassic igneous activities in the east flank of the East Kunlun orogenic belt: The Daheba complex example. *Int. Geol. Rev.* **2021**, 1–28. [CrossRef]

6. Tian, N.; Sun, F.Y.; Pan, Z.C.; Li, L.; Yan, J.M.; Wu, D.Q.; Gu, Y.; Zhang, Y. Petrogenesis and tectonic setting of Mid-Triassic volcanic rocks in the East Kunlun orogenic belt, NW China: Insights from geochemistry, zircon U–Pb dating, and Hf isotopes. *Geol. J.* **2021**, *56*, 3257–3274. [CrossRef]

7. Pan, G.T.; Wang, L.Q.; Li, R.S.; Yuan, S.H.; Ji, W.H.; Yin, F.G.; Zhang, W.P.; Wang, B.D. Tectonic evolution of the Qinghai-Tibet Plateau. *J. Asian Earth Sci.* **2012**, *53*, 3–14. [CrossRef]

8. Huang, H.; Niu, Y.L.; Nowell, G.; Zhao, Z.D.; Yu, X.H.; Zhu, D.C.; Mo, X.X.; Ding, S. Geochemical constraints on the petrogenesis of granitoids in the East Kunlun Orogenic belt, northern Tibetan Plateau: Implications for continental crust growth through syn-collisional felsic magmatism. *Chem. Geol.* **2014**, *370*, 1–18. [CrossRef]

9. Xiong, F.; Ma, C.Q.; Zhang, J.; Liu, B.; Jiang, H. Reworking of old continental lithosphere: An important crustal evolution mechanism in orogenic belts, as evidenced by Triassic I-type granitoids in the East Kunlun orogen, Northern Tibetan Plateau. *J. Geol. Soc. Lond.* **2014**, *171*, 847–863. [CrossRef]

10. Dong, Y.P.; He, D.F.; Sun, S.S.; Liu, X.M.; Zhou, X.H.; Zhang, F.F.; Yang, Z.; Cheng, B.; Zhao, G.C.; Li, J.H. Subduction and accretionary tectonics of the East Kunlun orogen, western segment of the Central China Orogenic System. *Earth Sci. Rev.* **2018**, *186*, 231–261. [CrossRef]

11. Liu, Y.J.; Genser, J.; Neubauer, F.; Jin, W.; Ge, X.H.; Handler, R.; Takasu, A. Ar-40/Ar-39 mineral ages from basement rocks in the Eastern Kunlun Mountains, NW China, and their tectonic implications. *Tectonophysics* **2005**, *398*, 199–224. [CrossRef]

12. Yuan, C.; Sun, M.; Xiao, W.J.; Wilde, S.; Li, X.H.; Liu, X.H.; Long, X.P.; Xia, X.P.; Ye, K.; Li, J.L. Garnet-bearing tonalitic porphyry from East Kunlun, Northeast Tibetan Plateau: Implications for adakite and magmas from the MASH Zone. *Int. J. Earth Sci.* **2009**, *98*, 1489–1510. [CrossRef]

13. Sun, F.Y.; Li, B.L.; Ding, Q.F.; Zhao, J.W.; Pan, T.; Yu, X.F.; Wang, L.; Chen, G.J.; Ding, Z.J. *Research on the Key Problems of Ore Prospecting in the Eastern Kunlun Metallogenic Belt*; Geological Survey Institute of Jilin University: Changchun, China, 2009. (In Chinese)

14. Yuan, C.; Zhou, M.F.; Sun, M.; Zhao, Y.; Wilde, S.; Long, X.; Yan, D. Triassic granitoids in the eastern Songpan Ganzi Fold Belt, SW China: Magmatic response to geodynamics of the deep lithosphere. *Earth Planet. Sci. Lett.* **2010**, *290*, 481–492. [CrossRef]

15. Liu, Y.S.; Gao, S.; Hu, Z.C.; Gao, C.G.; Zong, K.Q.; Wang, D.B. Continental and oceanic crust recycling-induced melt-peridotite interactions in the Trans-North China Orogen: U-Pb dating, Hf isotopes and trace elements in zircons of mantle xenoliths. *J. Petrol.* **2010**, *51*, 537–571. [CrossRef]

16. Ludwig, K.R. Isoplot 3.0: A geochronological toolkit for Microsoft Excel. *Berkeley Geochronol. Cent. Spec. Publ.* **2003**, *4*, 1–70.

17. Andersen, T. Correction of common lead in U–Pb analyses that do not report 204Pb. *Chem. Geol.* **2002**, *192*, 59–79. [CrossRef]

18. Wu, F.Y.; Yang, Y.H.; Xie, L.W.; Yang, J.H.; Xu, P. Hf isotopic compositions of the standard zircons and baddeleyites used in U–Pb geochronology. *Chem. Geol.* **2006**, *234*, 105–126. [CrossRef]

19. Pupin, J.P. Zircon and Granite Petrology. *Contrib. Mineral. Petrol.* **1980**, *73*, 207–220. [CrossRef]

20. Corfu, F.; Hanchar, J.M.; Hoskin, P.W.O.; Kinny, P. Atlas of Zircon Textures. *Rev. Mineral. Geochem.* **2003**, *53*, 469–500. [CrossRef]

21. Turkina, O.M.; Berezhnaya, N.G.; Lepekhina, E.N.; Kapitonov, I.N. U-Pb (SHRIMP-II), Lu–Hf isotope and trace element geochemistry of zircons from high-grade metamorphic rocks of the Irkut terrane, Sharyzhalgay Uplift: Implications for the Neoarchaean evolution of the Siberian Craton. *Gondwana Res.* **2012**, *21*, 801–817. [CrossRef]

22. Middlemost, E.A. Naming materials in the magma/igneous rock system. *Earth-Sci. Rev.* **1994**, *37*, 215–224. [CrossRef]

23. Peccerillo, A.; Taylor, S.R. Geochemistry of eocene calc-alkaline volcanic rocks from the Kastamonu area, Northern Turkey. *Contrib. Mineral. Petrol.* **1976**, *58*, 63–81. [CrossRef]

24. Maniar, P.D.; Piccoli, P.M. Tectonic discrimination of granitoids. *Geol. Soc. Am. Bull.* **1989**, *101*, 635–643. [CrossRef]

25. Frost, B.R.; Barnes, C.G.; Collins, W.J.; Arculus, R.J.; Ellis, D.J.; Frost, C.D. A Geochemical Classification for Granitic Rocks. *J. Petrol.* **2001**, *42*, 2033–2048. [CrossRef]

26. Taylor, S.R.; McLennan, S.M. *The Continental Crust: Its Composition and Evolution*; Blackwell Scientific Publications: Oxford, UK, 1985; pp. 91–92.

27. McDonough, W.F.; Sun, S.-S. The Composition of the Earth. *Chem. Geol.* **1995**, *120*, 223–253. [CrossRef]

28. Rudnick, R.L.; Gao, S. Composition of the continental crust. In *The Crust; Treatise on Geochemistry*; Holland, H.D., Turekian, K.K., Eds.; 2003; Volume 3, pp. 1–64.

29. Loiselle, M.C.; Wones, D.R. Characteristics and origin of anorogenic granites. *Geol. Soc. Am. Abst. Prog.* **1979**, *11*, 468.

30. Chappell, B.W.; White, A.J.R. Two contrasting granite types. *Pac. Geol.* **1974**, *8*, 173–174.

31. Collins, W.J.; Beams, S.D.; White, A.J.R.; Chappell, B.W. Nature and origin of A-type granites with particular reference to southeastern Australia. *Contrib. Miner. Pet.* **1982**, *80*, 189–200. [CrossRef]

32. Pearce, J.A.; Harris, N.B.W.; Tindle, A.G. Trace Element Discrimination Diagrams for the Tectonic Interpretation of Granitic Rocks. *J. Petrol.* **1984**, *25*, 956–983. [CrossRef]

33. Pitcher, W. Granite type and tectonic environment. In Proceedings of the Symposium on Mountain Building, Princeton, NJ, USA, 9–12 May 1983; pp. 19–40.

34. Whalen, J.B.; Currie, K.L.; Chappell, B.W. A-type granites: Geochemical characteristics, discriminatuon and petrogenesis. *Contrib. Mineral. Petrol.* **1987**, *95*, 407–419. [CrossRef]

35. Wu, F.Y.; Jahn, B.M.; Wilde, S.A.; Lo, C.H.; Yui, T.F.; Lin, Q.; Ge, W.C.; Sun, D.Y. Highly fractionated I-type granites in NE China (I): Geochronology and petrogenesis. *Lithos* **2003**, *66*, 241–273. [CrossRef]

36. Wu, F.Y.; Jahn, B.M.; Wilde, S.A.; Lo, C.H.; Yui, T.F.; Lin, Q.; Ge, W.C.; Sun, D.Y. Highly fractionated I-type granites in NE China (II): Isotopic geochemistry and implications for crustal growth in the Phanerozoic. *Lithos* **2003**, *67*, 191–204. [CrossRef]

37. Wu, F.Y.; Li, X.H.; Yang, J.H.; Zheng, Y.F. Discussion on the petrogenesis of granites. *Acta Petrol. Sin.* **2007**, *23*, 1217–1238.

38. White, A.J.R. Sources of granite magmas. *Geol. Soc. Am.* **1979**, *11*, 539.

39. Whalen, J.B. Geochemistry of an island-arc plutonic suite: The Uasilau-Yau Yau intrusive complex, New Britain, P.N.G. *J. Petrol.* **1985**, *26*, 603–632. [CrossRef]

40. Douce, A.E.P. Generation of metaluminous A-type granites by low-pressure melting of calc-alkaline granitoids. *Geology* **1997**, *25*, 743–746. [CrossRef]

41. King, P.L.; White, A.J.R.; Chappell, B.W.; Allen, C.M. Characterization and origin of aluminous A-type granites from the Lachlan fold belt, southeastern Australia. *J. Petrol.* **1997**, *38*, 371–391. [CrossRef]

42. Watson, E.B.; Harrison, T.M. Zircon saturation revisited: Temperature and composition effects in a variety of crustal magma types. *Earth Planet. Sci. Lett.* **1983**, *2*, 295–304. [CrossRef]

43. Chappell, B.W. Aluminium saturation in I- and S-type granites and the characterization of fractionated haplogranites. *Lithos* **1999**, *46*, 535–551. [CrossRef]

44. Chappell, B.W.; White, A.J.R. I-and S-type granites in the Lachlan Fold Belt. *Earth Environ. Sci. Trans. R. Soc. Edinb.* **1992**, *83*, 1–26.

45. Zorpi, M.J.; Coulon, C.; Orsini, J.B. Hybridization between felsic and mafic magmas in calc-alkaline granitoids—A case study in northern Sardinia, Italy. *Chem. Geol.* **1991**, *92*, 45–86. [CrossRef]

46. Hoffmann, J.E.; Münker, C.; Polat, A.; Rosing, M.T.; Schulz, T. The origin of decoupled Hf-Nd isotope compositions in Eoarchean rocks from southern west Greenland. *Geochim. Cosmochim. Acta.* **2011**, *75*, 6610–6628. [CrossRef]

47. Barbarin, B. Genesis of the two main types of peraluminous granitoids. *Geology* **1996**, *24*, 295–298. [CrossRef]

48. Wu, T.; Zhou, J.X.; Wang, X.C.; Li, W.X.; Wilde, S.A.; Sun, H.R.; Wang, J.S.; Li, Z. Identification of Ca. 850 Ma High-Temperature Strongly Peraluminous Granitoids in Southeastern Guizhou Province, South China: A Result of Early Extension Along the Southern Margin of the Yangtze Block. *Precambrian Res.* **2018**, *308*, 18–34. [CrossRef]

49. Sisson, T.W. Hornblende-Melt Trace-Element Partitioning Measured by Ion Microprobe. *Chem. Geol.* **1994**, *117*, 331–334. [CrossRef]

50. Słaby, E.; Götze, J.; Wörner, G.; Simon, K.; Wrzalik, R.; Śmigielski, M. K-feldspar phenocrysts in microgranular magmatic enclaves: A cathodoluminescence and geochemical study of crystal growth as a marker of magma mingling dynamics. *Lithos* **2008**, *105*, 85–97. [CrossRef]

51. Vernon, R.H. Granites really are magmatic: Using microstructural evidence to refute some obstinate hypotheses. *J. Virtual Explor.* **2010**, *35*, 1–36. [CrossRef]

52. Barbarin, B. Mafic magmatic enclaves and mafic rocks associated with some granitoids of the central Sierra Nevada batholith, California: Nature, origin, and relations with the hosts. *Lithos* **2005**, *80*, 155–177. [CrossRef]

53. Rapp, R.P.; Watson, E.B. Dehydration melting of metabasalt at 8–32 kbar: Implications for continental growth and crust-mantle recycling. *J. Petrol.* **1995**, *36*, 891–931. [CrossRef]

54. Lu, S.N.; Li, H.K.; Wang, H.C.; Chen, Z.H.; Zheng, J.K.; Xiang, Z.Q. Detrital zircon population of Proterozoic meta-sedimentary strata in the Qinling-Qilian-Kunlun Orogen. *Acta Petrol. Sin.* **2009**, *25*, 2195–2208.

55. Taniuchi, H.; Kuritani, T.; Nakagawa, M. Generation of Calc-Alkaline Andesite Magma through Crustal Melting Induced by Emplacement of Mantle-Derived Water-Rich Primary Magma: Evidence From Rishiri Volcano, Southern Kuril Arc. *Lithos* **2020**, *354–355*, 105362. [CrossRef]

56. Hirose, K. Melting Experiments On Lherzolite KLB-1 Under Hydrous Conditions and Generation of High-Magnesian Andesitic Melts. *Geology* **1997**, *25*, 42–44. [CrossRef]

57. Tamura, Y.; Sato, T.; Fujiwara, T.; Kodaira, S.; Nichols, A. Advent of Continents: A New Hypothesis. *Sci. Rep.* **2016**, *6*, 1–12.

58. Bellieni, G.; Cavazzini, G.; Fioretti, A.M.; Peccerillo, A.; Poli, G. Geochemical and isotopic evidence for crystal fractionation, AFC and crustal anatexis in the genesis of the Rensen Plutonic Complex (Eastern Alps, Italy). *Contrib. Miner. Petrol.* **1991**, *92*, 21–43. [CrossRef]

59. Sisson, T.W.; Grove, T.L. Experimental Investigations of the Role of H$_2$O in Calc-Alkaline Differentiation and Subduction Zone Magmatism. *Contrib. Mineral. Petrol.* **1993**, *113*, 143–166. [CrossRef]

60. Kepezhinskas, P.; Defant, M.J.; Drummond, M.S. Progressive Enrichment of Island Arc Mantle by Melt-Peridotite Interaction Inferred From Kamchatka Xenoliths. *Geochim. et Cosmochim. Acta* **1996**, *60*, 1217–1229. [CrossRef]

61. Gao, S.; Rudnick, R.L.; Yuan, H.L.; Liu, X.M.; Liu, Y.S.; Xu, W.L.; Ling, W.L.; Ayers, J.; Wang, X.C.; Wang, Q.H. Recycling Lower Continental Crust in the North China Craton. *Nature* **2004**, *432*, 892–897. [CrossRef]

62. Petford, N.; Atherton, M. Na-Rich Partial Melts From Newly Underplated Basaltic Crust; The Cordillera Blanca Batholith, Peru. *J. Petrol.* **1996**, *37*, 1491–1521. [CrossRef]

63. Sakuyama, M. Petrological Study of the Myoko and Kurohime Volcanoes, Japan; Crystallization Sequence and Evidence for Magma Mixing. *J. Petrol.* **1981**, *22*, 553–583. [CrossRef]

64. Kushiro, I. Partial melting of mantle wedge and evolution of island arc crust. *J. Geophys. Res.* **1990**, *95*, 15929–15939. [CrossRef]

65. Defant, M.J.; Drummond, M.S. Derivation of some modern arc magmas by melting of young subducted lithosphere. *Nature* **1990**, *347*, 662–665. [CrossRef]

66. Sun, S.S.; McDonough, W.F. Chemical and isotopic systematics of oceanic basalts: Implications for mantle composition and processes. *Geol. Soc. Lond. Spec. Publ.* **1989**, *42*, 313–345. [CrossRef]

67. Taylor, S.R.; McLennan, S.M. The Geochemical Evolution of the Continental Crust. *Rev. Geophys.* **1995**, *33*, 241–265. [CrossRef]

68. Martin, H. Adakitic magmas: Modern analogues of Archaean granitoids. *Lithos* **1999**, *46*, 411–429. [CrossRef]

69. Xu, Z.H.; Xin, W.; Zhou, X.D.; Xu, Q.L.; Li, F.W.; Song, Z.J. Triassic granitoids in the East Kunlun Orogenic Belt, Northwestern China: Magmatic source and implications for geodynamic evolution. *Int. Geol. Rev.* **2020**, 1–17. [CrossRef]

70. Xia, R.; Wang, C.M.; Deng, J.; Carranza, E.J.M.; Li, W.; Qing, M. Crustal theckening prior to 220 Ma in the East Kunlun Orogenic Belt: Insights from Late Triassic granitoids in the Xiao-Nuomuhong pluton. *J. Asian Earth Sci.* **2014**, *93*, 193–210. [CrossRef]

71. Zhang, Q.; Pan, G.Q.; Li, C.D.; Jin, W.J.; Jia, X.Q. Granitic magma mixing versus basaltic magma mixing: New viewpoints on granitic magma mixing process: Some crucial questions on granite study. *Acta Petrol. Sin.* **2007**, *23*, 1141–1152. (In Chinese with English abstract)

72. Wang, Y.W.; Wang, J.B.; Long, L.L.; Zou, T.; Tang, P.Z.; Wang, L.J. Type, indicator, mechanism, model and relationship with mineralization of magma mixing: A case study in North Xinjiang. *Acta Petrol. Sin.* **2012**, *28*, 2317–2330. (In Chinese with English abstract)

73. Li, R.B.; Pei, X.Z.; Li, Z.C.; Liu, Z.Q.; Chen, G.C.; Chen, Y.X.; Wei, F.H.; Gao, J.M.; Liu, C.J.; Pei, L. Geological characteristics of Late Paleozoic-Mesozoic unconformities and their response to some significiant tectonic events in eastern part of Eastern Kunlun. *Earth Sci. Front.* **2012**, *19*, 244–254. (In Chinese with English abstract)

74. Chen, S.J.; Li, R.S.; Ji, W.H.; Zhao, Z.M.; Liu, R.L.; Jia, B.H.; Zhang, Z.F.; Wang, G.C. The Permian lithofacies paleogeographic characteristics and basin-mountain conversion in the Kunlun orogenic belt. *Geol. China* **2010**, *37*, 374–393. (In Chinese with English abstract)

75. Yang, J.S.; Shi, R.D.; Wu, C.L.; Wang, X.B.; Robinson, P. Dur'ngoi ophiolite in East Kunlun, Northeast Tibetan plateau: Evidence for paleo-Tethyan suture in Northwest China. *J. Earth Sci.* **2009**, *20*, 303–331. [CrossRef]

76. Liu, Z.Q.; Pei, X.Z.; Li, R.B.; Li, Z.C.; Zhang, X.F.; Liu, Z.G.; Chen, G.C.; Chen, Y.X.; Ding, S.P.; Guo, J.F. LA-ICP-MS Zircon U-Pb Geochronology of the two Suites of Ophiolites at the Buqingshan Area of the A'nyemaqen Orogenic Belt in the Southern margin of East Kunlun and its Tectonic Implication. *Acta Geol. Sin.* **2011**, *30*, 185–194. (In Chinese with English abstract)

77. Yang, Y.Q.; Li, B.L.; Xu, Q.L.; Zhang, B.S. Zircon U-Pb ages and its geological significance of the monzonitic granite in the Aikengdelesite, Eastern Kunlun. *Northwestern Geol.* **2013**, *46*, 56–62. (In Chinese with English abstract)

78. Chen, B.X.; Xu, S.L.; Yang, Y.S.; Zhou, N.W.; Zhu, Z.X. Genesis and tectonic significance of Late Permian Qimulaike intrusiverocks in the west of East Kunlun Mountains, Xinjiang. *Geol. Bull. China* **2019**, *38*, 1040–1051. (In Chinese with English abstract)

79. Xiong, F.H.; Ma, C.Q.; Zhang, J.Y.; Liu, B. LA-ICP-MS zircon U-Pb dating, elements and Sr-Nd-Hf isotope geochemistry of the Early Mesozoic mafic dike swarm in East Kunlun orogenic belt. *Acta Petrol.* **2011**, *27*, 3350–3364.

80. Xiong, F.H.; Ma, C.Q.; Jiang, H.A.; Liu, B.; Zhang, J.Y.; Zhou, Q. Petrogenetic and tectonic significance of Permian calc-alkaline lamprophyres, East Kunlun OrogenicBelt, northern Qinghai-Tibet plateau. *Int. Geol. Rev.* **2013**, *55*, 1817–1834. [CrossRef]

81. Li, R.B.; Pei, X.Z.; Li, Z.C.; Pei, L.; Chen, G.C.; Chen, Y.X.; Liu, C.J.; Wang, S.M. Paleo-Tethys Ocean subduction in eastern section of East Kunlun Orogen: Evidence from the geochronology and geochemistry of the Wutuo pluton. *Acta Petrol. Sin.* **2018**, *34*, 3399–3421.

82. Hoek, J.D.; Seitz, H.M. Continental mafic dike swarm as tectonic indicators: An example from the Vestfold Hills, East Antarctica. *Precambrian Res.* **1995**, *75*, 121–139. [CrossRef]

83. Garfunkel, Z.; Anderson, C.A.; Schubert, G. Mantle circulation and the lateral migration of subducted slabs. *J. Geophys. Res. Solid Earth* **1986**, *91*, 7205–7223. [CrossRef]

84. Gill, J.B. Andesite Genesis. (Book Reviews: Orogenic Andesitesand Plate Tectonics). *Science* **1982**, *218*, 1111–1112.

85. Wilson, M. *Igneous Petrogenesis*; Unwin Hyman: London, UK, 1989; pp. 1–25.

86. Salters, V.J.M.; Hart, S.R. The mantle sources of ocean ridges, islands and arcs; the Hf-isotope connection. *Earth Planet. Sci. Lett.* **1991**, *104*, 364–380. [CrossRef]

87. Li, S.M.; Zhu, D.C.; Wang, Q.; Zhao, Z.D.; Sui, Q.L.; Liu, S.A.; Liu, D.; Mo, X.X. Northward subduction of Bangong–Nujiang Tethys: Insight from Late Jurassic intrusive rocks from Bangong Tso in western Tibet. *Lithos* **2014**, *205*, 284–297. [CrossRef]

88. Chen, G.C.; Pei, X.Z.; Li, R.B.; Li, Z.C.; Liu, C.J.; Chen, Y.X.; Pei, L.; Zang, Y.M.; Wang, M.; Li, X.B.; et al. Age and petrogenesis of Jialuhe basic—Intermediate pluton in Xiangjia'nanshan granite batholith in the eastern part of East Kunlun Orogenic Belt, and its geological significance. *Geotecton Metallog.* **2017**, *41*, 1097–1115. (In Chinese with English abstract)

89. Chen, G.C.; Pei, X.Z.; Li, R.B.; Li, Z.C.; Pei, L.; Liu, C.J.; Chen, Y.X.; Li, X.B. Triassic magma mixing and mingling at the the eastern section of Eastern Kunlun: A case study from Xiangjiananshan granitic batholith. *Acta Petrol. Sin.* **2018**, *34*, 2441–2480. (In Chinese with English abstract)

90. Fan, X.Z.; Sun, F.Y.; Xu, C.H.; Wu, D.Q.; Yu, L.; Wang, L.; Yan, C.; Baknt, S. Volcanic rocks of the Elashan Formation in the Dulan-Xiangride Basin, East Kunlun Orogenic Belt, NW China: Petrogenesis and implications for Late Triassic geodynamic evolution. *Int. Geol. Rev.* **2021**, *64*, 1270–1293. [CrossRef]